Article
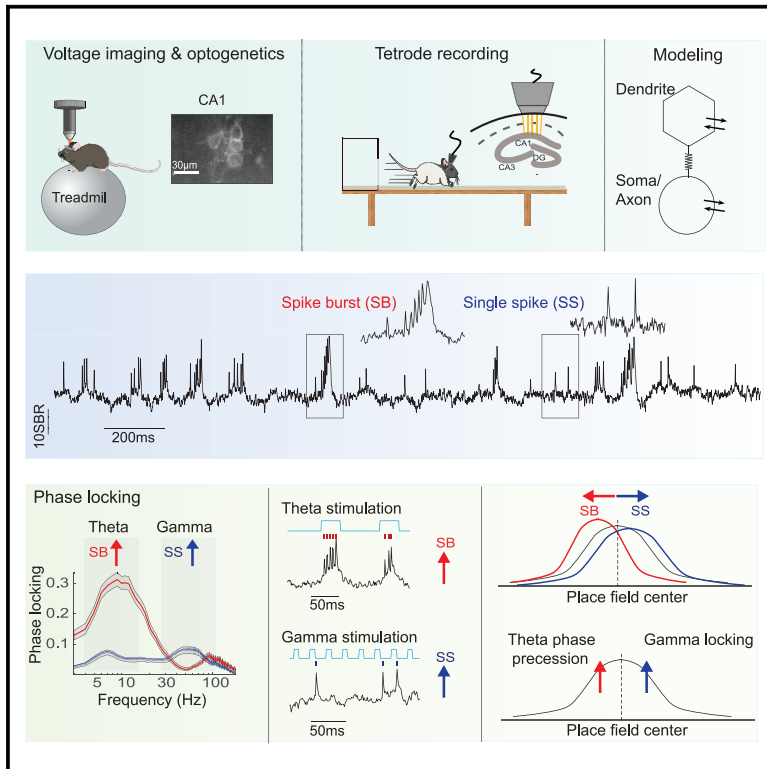
Theta and gamma rhythmic coding through two spike output modes in the hippocampus during spatial navigation

Graphical abstract

Highlights

- Single spikes (SSs) and spike bursts (SBs) are coupled to theta versus gamma rhythms

- Single cell subthreshold theta and gamma inputs determine SB and SS generation

- SSs and SBs exhibit distinct coding properties during spatial navigation

- Cellular biophysical properties are sufficient to support distinct SS and SB coding

Authors

Eric Lowet, Daniel J. Sheehan, Ulises Chialva, ..., Michael E. Hasselmo, Horacio G. Rotstein, Xue Han

Correspondence

elowet@mailfence.com (E.L.),
xuehan@bu.edu (X.H.)

In brief

By combining tetrode recordings in navigating rats, cellular voltage imaging in awake mice, and biophysical modeling, Lowet et al. show that hippocampal CA1 neurons exhibit two output modes, spike bursts and single spikes, which are differently regulated by theta versus gamma frequency inputs and provide complementary spatial coding during navigation.

CellPress

Cell Reports

OPEN ACCESS

Article

Theta and gamma rhythmic coding through two spike output modes in the hippocampus during spatial navigation

Eric Lowet,[1,*] Daniel J. Sheehan,[2,8] Ulises Chialva,[3,8] Rodrigo De Oliveira Pena,[4,8] Rebecca A. Mount,[1] Sheng Xiao,[1] Samuel L. Zhou,[1] Hua-an Tseng,[1] Howard Gritton,[5] Sanaya Shroff,[1] Krishnakanth Kondabolu,[1] Cyrus Cheung,[1] Yangyang Wang,[1] Kiryl D. Piatkevich,[6] Edward S. Boyden,[7] Jerome Mertz,[1] Michael E. Hasselmo,[2] Horacio G. Rotstein,[4] and Xue Han[1,9,*]

[1]Department of Biomedical Engineering, Boston University, Boston, MA, USA
[2]Department of Psychological and Brain Sciences, Boston University, Boston, MA, USA
[3]Departamento de Matemática, Universidad Nacional del Sur, Buenos Aires, Argentina
[4]Federated Department of Biological Sciences, New Jersey Institute of Technology & Rutgers University, Newark, NJ, USA
[5]Department of Comparative Biosciences, University of Illinois at Urbana–Champaign, Urbana, IL, USA
[6]School of Life Sciences, Westlake University, Westlake Laboratory of Life Sciences and Biomedicine, Westlake Institute for Advanced Study, Hangzhou, Zhejiang, China
[7]McGovern Institute for Brain Research and Howard Hughes Medical Institute, MIT, Cambridge, MA, USA
[8]These authors contributed equally
[9]Lead contact
*Correspondence: elowet@mailfence.com (E.L.), xuehan@bu.edu (X.H.)
https://doi.org/10.1016/j.celrep.2023.112906

SUMMARY

Hippocampal CA1 neurons generate single spikes and stereotyped bursts of spikes. However, it is unclear how individual neurons dynamically switch between these output modes and whether these two spiking outputs relay distinct information. We performed extracellular recordings in spatially navigating rats and cellular voltage imaging and optogenetics in awake mice. We found that spike bursts are preferentially linked to cellular and network theta rhythms (3–12 Hz) and encode an animal's position via theta phase precession, particularly as animals are entering a place field. In contrast, single spikes exhibit additional coupling to gamma rhythms (30–100 Hz), particularly as animals leave a place field. Biophysical modeling suggests that intracellular properties alone are sufficient to explain the observed input frequency-dependent spike coding. Thus, hippocampal neurons regulate the generation of bursts and single spikes according to frequency-specific network and intracellular dynamics, suggesting that these spiking modes perform distinct computations to support spatial behavior.

INTRODUCTION

Neurons in many brain circuits, including the cerebellum, hippocampus, and thalamus, produce spike bursts[1–5] (SBs) that are important for synaptic plasticity[6–8] and information transfer.[2,9,10] In the hippocampus, SBs are thought to reflect the unique intracellular events known as complex spikes, which consist of several action potentials riding on top of large amplitude subthreshold membrane depolarizations.[3,11–13] Patch-clamp recordings have revealed that complex spikes are not simply a cluster of rapidly occurring single spikes (SSs), but rather involve distinct membrane voltage mechanisms that support the prominent subthreshold depolarizations accompanying SBs.[3,5,6,11,14] The unique subthreshold membrane depolarization during complex spikes recruits specific voltage-dependent membrane currents,[15] resulting in long-lasting dendritic plateau potentials.[6,10,16] These have been shown to be critical for circuit plasticity, including CA1 place field formation as well as modu-

lating network information processing and transmission.[3,17] Because of the tight coupling of high-frequency spiking and prominent subthreshold dynamics, SBs have also been linked to hippocampus-dependent pathologies, e.g., temporal lobe epilepsy.[18–20] While the cellular and synaptic effects of SBs and SSs are well studied, their role in network computation during behavior remains unclear.

Action potential generation is determined by the somatic membrane voltage that reflects a spatiotemporal integration of dendritic inputs, particularly coordinated inputs from local and distal circuits. Network coordination is commonly assessed by recording extracellular local field potentials (LFPs), where correlated synaptic inputs are reflected in the LFP rhythms. In the hippocampus, LFPs show prominent theta (~5–10 Hz)[21–25] and gamma (~30–100 Hz) rhythms[26–30] that are broadly linked to learning and memory. CA1 receives two major input sources that originate from CA3 and the entorhinal cortex (EC). CA3 and EC inputs converge onto CA1 pyramidal neurons in a theta phase

coordinated manner.[16,27,28] Additionally, these inputs exhibit different gamma rhythms across the slow (30–50 Hz), middle (60–100 Hz), and fast (>100 Hz) frequencies and are thought to contribute to layer-dependent CA1 gamma rhythms.[27,28] While both hippocampal theta- and gamma-band activities have been shown to modulate spike timing during behavior, it is unclear how these rhythms influence SB and SS generation and whether they perform different network computation.

We analyzed extracellularly recorded SBs and SSs from dorsal CA1 neurons in spatially navigating rats and discovered that these two outputs are differentially related to network theta and gamma rhythms and exhibit distinct place field coding properties. To understand the cellular mechanisms, we performed cellular SomArchon[31] voltage imaging from individual CA1 neurons while simultaneously recording LFPs in awake mice. SomArchon voltage imaging, like intracellular recordings, can resolve subthreshold membrane voltage that cannot be measured by extracellular recordings.[5,31–35] We found that SBs and SSs are differentially regulated by cellular theta and gamma rhythmicity, and subthreshold membrane voltage dynamics are coordinated with network LFP rhythms. Exploiting the wavelength compatibility of near-infrared SomArchon voltage imaging with blue-light optogenetics, we revealed a causal role of rhythmic membrane voltage in modulating SB and SS probability. Finally, we recapitulated the experimental results using biophysical models and confirmed that intrinsic membrane ion channel kinetics are sufficient to explain the frequency-specific coding of SBs and SSs.

RESULTS

CA1 SBs and SSs are differentially associated with LFP theta and gamma oscillations during spatial navigation in rats

Hippocampal CA1 neurons have place fields,[36,37] and CA1 spiking has been widely related to theta and gamma rhythms.[36,38] However, it remains unclear how SSs and SBs relate to CA1 rhythms and contribute to place field coding. We first analyzed SBs and SSs in dorsal CA1 recorded with tetrodes in navigating rats. Rats were trained to run bidirectionally relative to a home box, on a custom-built 180-cm-long wooden linear track in a room with environmental cues (Figures 1A and 1B). Because place field structures vary depending on whether the rats ran in the inbound or the outbound direction,[24] we used the firing rate of each place cell in the direction that exhibited the strongest modulation calculated using all spikes (see STAR Methods). Neurons with firing rates of >20 Hz, presumably fast-spiking interneurons, were excluded from the analysis. For place field analysis, we only included neurons with a spatial information index of >0.2 (see STAR Methods).

The firing rate for the entire recording duration was 1.1 ± 2.1 Hz (median $\pm$ standard deviation; n = 147), with a peak firing of 1.9 ± 4.4 Hz (STAR Methods). We separated SBs from SSs using an interspike interval (ISI)-based criterion of <10 ms[39,40] (Figures 1C, S1A, and S1B). We found that $28.8\% \pm 13.9\%$ (median $\pm$ standard deviation; n = 147 neurons) of all recorded spikes were SBs (counting all spikes within an SB) (Figure 1C). To examine how SBs and SSs are linked to LFP rhythms, we

calculated spike-LFP phase-locking strength ($PLVu^2$, adjusted for spike numbers; see STAR Methods), which measures the phase consistency of spikes. Specifically, we computed the $PLVu^2$ of SSs or SBs relative to the LFP theta (5–12 Hz) phase for each neuron, and then averaged across all neurons. We observed that SBs exhibited several-fold stronger spike-LFP $PLVu^2$ at theta frequencies than SSs (Figures 1D–1G), consistent with a previous study.[40] As each SB event contains multiple individual spikes, the number of spikes within an SB could impact the phase locking measure. We thus computed the spike-LFP $PLVu^2$ using only the first spike within each SB, which also showed stronger theta phase preference than SSs (Figures S1C and S1D). Moreover, spike-LFP theta $PLVu^2$ increased with the number of spikes contained within an SB (Figure 1H). Compared to SBs, SSs were additionally associated with LFP gamma rhythms (Figure 1D–1G), with a peak in the mid-gamma range ($\sim$70–100 Hz) (Figure 1F) that has been associated with EC inputs.[28]

Because of the overlapping ISI distribution of SBs and SSs, SB classification using ISI thresholding alone results in inherent inaccuracies. Thus, we further explored how different ISI thresholds influence the observed SB and SS differences. We identified SBs using different ISI thresholds that have been generally reported in the literature (6–15 ms) and found that the observed preference of SB and SS phase locking to LFP theta versus gamma was largely independent of the ISI thresholds chosen (Figures S2A–S2F). Additionally, we identified SBs using a surprise-based algorithm[41] detecting deviations from the expected Poisson firing rate distribution (see STAR Methods), which again led to similar findings (Figures S2G–S2I). Matching the spike number of SBs and SSs further confirmed the observed differences (Figures S2J–S2L). Finally, we analyzed the Allen Brain Institute's CA1 spiking data recorded with Neuropixels probes in head-fixed behaving mice (see STAR Methods). We found that $26.6\% \pm 23.4\%$ (median $\pm$ standard deviation; n = 1,689 neurons) of recorded spikes were SBs, strikingly similar to the 28.8% observed in our rat tetrode data (Figure 1C). Interestingly, the overall spike rate of CA1 neurons in head-fixed mice was 5.1 ± 8.46 Hz (median $\pm$ standard deviation; n = 1,689), higher than that observed in our spatially navigating rats (1.1 Hz), but similar to what we observed with cellular voltage imaging in head-fixed mice (5.8 ± 6.1 Hz, median $\pm$ standard deviation, n = 56; for details, see Results related to Figure 3). Further, we found the same differential coupling of SBs and SSs to LFP rhythms (Figures S2M–S2R).

SBs and SSs exhibit distinct coding properties during spatial navigation

CA1 theta and gamma oscillations have been broadly linked to distinct behavioral functions.[21,30] The preferred association of CA1 LFP theta to SBs and LFP gamma to SSs during spatial navigation suggests that SBs and SSs may also exhibit different spatial coding properties. Thus, we compared how SB and SS firing rates were modulated by spatial location by calculating the ratio of peak firing rate to the mean firing rate for each neuron (Figure 2A). Interestingly, SB firing rate modulation was significantly greater than SS as animals ran through the place field of the neuron (Figure 2B). Further, SBs carried greater spatial information than SSs (Figure 2C), regardless of the variability in the
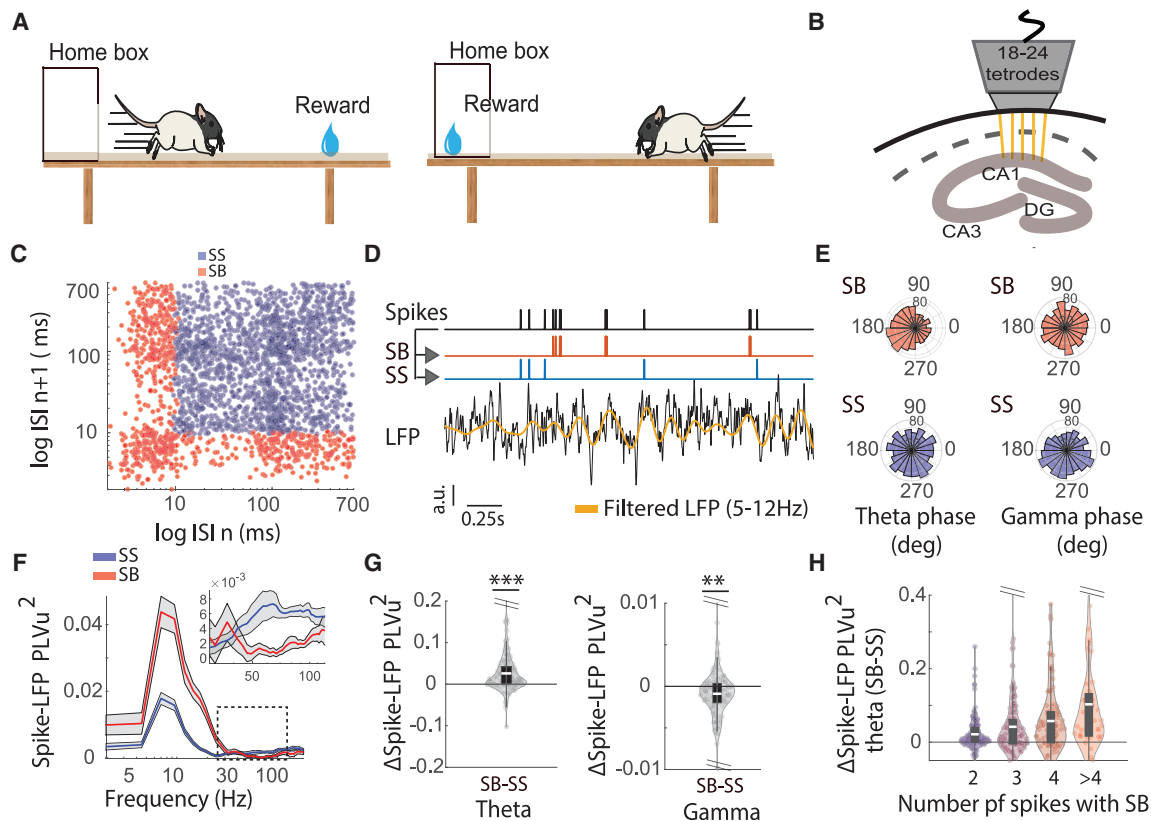
Figure 1. SSs and SBs differentially phase lock to LFP theta and gamma oscillations in the rat hippocampal CA1

(A) Schematic of the behavioral setup.

(B) Schematic of the extracellular tetrodes placed in the dorsal CA1.

(C) ISI return map (ISI n vs. ISI n + 1) depicting the ISI distributions (log scale) for SBs (red) and SSs (blue).

(D) An example LFP trace (black, and theta filtered in gold) and the simultaneously recorded spike train (black) with every spike classified as either a SB (red) or a SS (blue).

(E) Polar histograms of SBs (top) and SSs (bottom) phase relative to LFP theta (left) or gamma (right) for the example neuron shown in (D).

(F and G) (F) Population averaged spike-LFP $PLVu^2$ across frequencies (n = 147 neurons) (G). The difference of SB-LFP $PLVu^2$ and SS-LFP $PLVu^2$ at theta (5–12 Hz) and gamma (30–100 Hz) ranges. SB-LFP theta $PLVu^2$ is significantly higher than SS (one-sample t test, $p < 1 \times 10^{-20}$, df = 146). SS-LFP gamma $PLVu^2$ is significantly higher than SB (one-sample t test, $p = 1.3 \times 10^{-15}$, df = 146).

(H) Quantification of SB-LFP theta $PLVu^2$ for SB events containing an increasing number of spikes (linear regression slope, $p < 1 \times 10^{-20}$; n = 66 SB events). For each neuron, the SB $PLVu^2$ were subtracted by the SS $PLVu^2$ values. ***$p < 0.001$; **$p < 0.01$.

number of SBs and SSs in each neuron (Figures S3A–S3C). Finally, we noticed that SBs often occurred earlier than SSs within the place field for a given direction (Figures 2D and S3D–S3F). Direct comparison of this spatial difference between SB and SS firing rate using a center of mass (COM) calculation revealed that SB firing occurred significantly earlier than SS (Figure 2E), suggesting that SBs were more prevalent when an animal entered the place field, whereas SSs were prevalent as an animal left the place field.

Another prominent phenomenon of CA1 spatial coding is theta phase precession.[21,25] We, therefore, calculated the preferred phase of SBs (all spikes within SB) and SSs relative to LFP theta at each spatial location (Figure 2F) and computed the circular-linear correlation between the spike-LFP theta phase and the spatial position. We found that SBs exhibited stronger correlations with spatial position than SSs (Figure 2G). Moreover, in line with the place field asymmetry of SBs and SSs (Figure 2E),

SB theta locking was stronger in the first half of the place field (Figures 2H and 2I), whereas SS gamma locking was stronger in the second half (Figures 2J and 2K). Thus, SBs and SSs contribute distinctively to neurons' place field structures, depending on network oscillation states.

Intracellularly recorded complex SBs are associated with substantial membrane voltage depolarizations that contribute to subthreshold theta power

Since extracellular tetrode recordings do not provide access to membrane voltage, intracellular recordings are required to probe the cellular voltage mechanisms of the observed differential association of SSs and SBs to network rhythms. We, therefore, performed SomArchon[31] voltage imaging from individual CA1 neurons while simultaneously recording LFPs in awake mice. SomArchon is a fully genetically encoded, soma-targeted voltage sensor whose near-infrared fluorescence is linearly
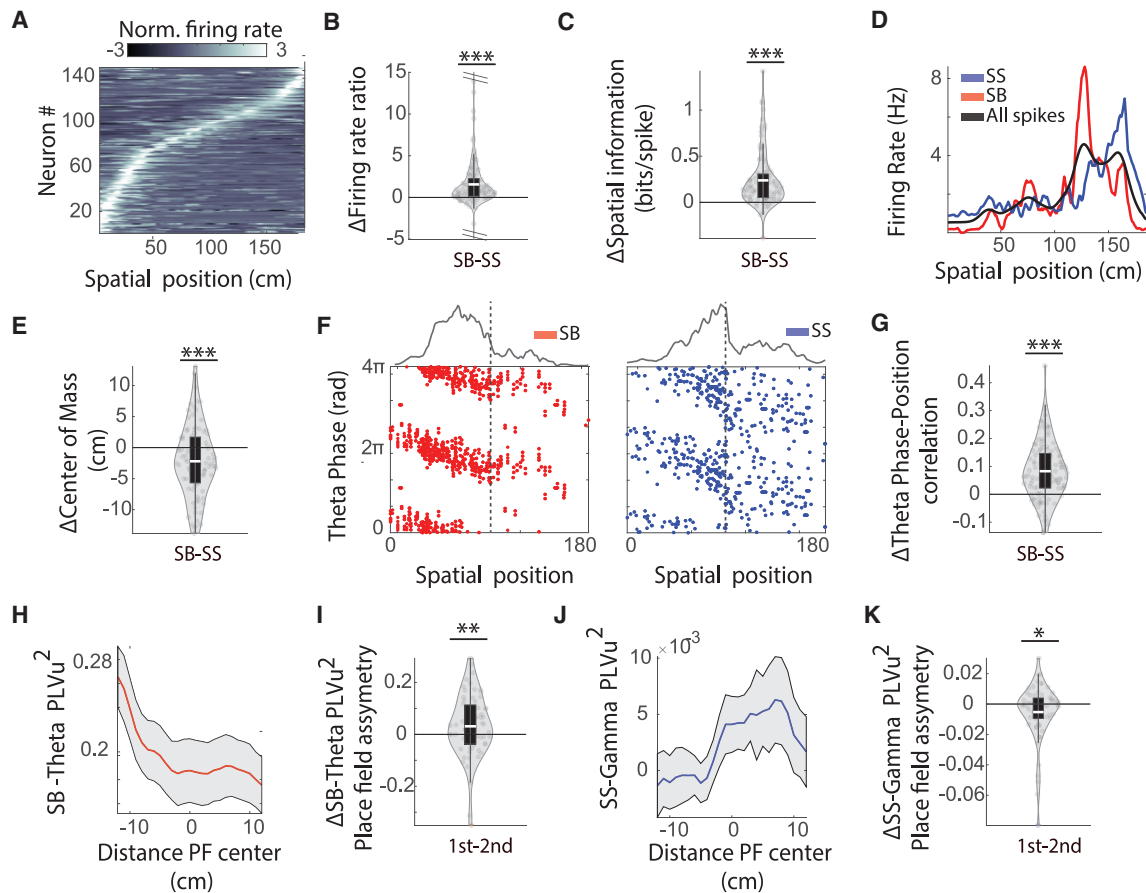
Figure 2. Distinct spatial coding and phase precession properties of SSs and SBs during spatial navigation in rats

(A) Normalized firing rate (all spikes), *Z* scored over animal's position. Neurons are sorted based on the location of their peak firing rate.

(B and C) (B) The difference in SB and SS firing rate modulation, calculated as the ratio of the peak firing rate relative to the mean firing rate. SB firing rate modulation was significantly stronger than SS firing rate modulation (p = 3.6 × 10^{-8}; n = 147 neurons) (C). The difference in SB and SS spatial information metric, calculated as bits per spike.

(D) An example neuron's spike rate over spatial location, calculated using SBs (red), SSs (blue), or all spikes (black).

(E) The difference of neurons' place field center calculated using COM. The COMs for SBs are significantly lower (closer to starting point) than SSs (p = 3.9 × 10^{-4}; n = 91 neurons with COMs within 10 cm of the COMs estimated using all spikes).

(F) An example CA1 neuron's spike times relative to LFP theta phase over the animal's spatial position for SBs (red) and SSs (blue). Each dot indicates a spike, and the spike histogram is on the top.

(G) The difference in circular-linear correlation values between SB and SS spike phase relative to LFP theta oscillations (5–12 Hz) and animal's spatial position. SBs show stronger correlations with spatial position than SSs (p = 1.8 × 10^{-13}, df = 130).

(H) Population averaged SB-LFP theta PLVu^2 aligned to the SB place field (PF) center of each neuron.

(I) The difference in the mean SB-LFP theta PLVu^2 during the first and second halves of the PF. SB -LFP theta PLVu^2 is significantly higher for the first half of the PF than the second half (p = 0.007; n = 63 neurons with >10 spikes).

(J and K) Same as (H) and (I), but for spike-LFP gamma PLVu^2. SB-LFP gamma PLVu^2 is significantly lower for the first half of the PF than the second half (p = 0.04; n = 63). All statistics are two-sided one-sample t tests. ***p < 0.001; **p < 0.01; *p < 0.05.

related to membrane voltage from −100 to +60 mV,[31] allowing for reliable measurement of individual spikes and subthreshold membrane voltage (Vm) at the soma.[32–35] Further, SomArchon is compatible with the blue light-driven channelrhodopsin CoChR for causal analysis of cellular Vm dynamics.

We surgically implanted an imaging window coupled with an infusion cannula and an LFP electrode, and infused AAV9-Syn-SomArchon-p2A-CoChR-Kv2.1 into CA1. During recording sessions, habituated animals were head-fixed under a microscope on a Styrofoam ball supported by air (Figure 3A). To examine

how subthreshold dynamics influence spike timing, we removed identified spikes from SomArchon traces to obtain the subthreshold Vm trace for each neuron (see STAR Methods).

We observed that many neurons produced clusters of spikes riding on top of substantial Vm depolarization (Figure 3B), consistent with the classically described complex spikes in intracellular studies.[3,11,14] With the ability to record Vm, SBs can thus be identified more reliably using not only ISI, but also after-depolarization potentials (ADPs) (see STAR Methods). Using combined ISI and ADP criteria, we found that 28.2% ± 17.1%
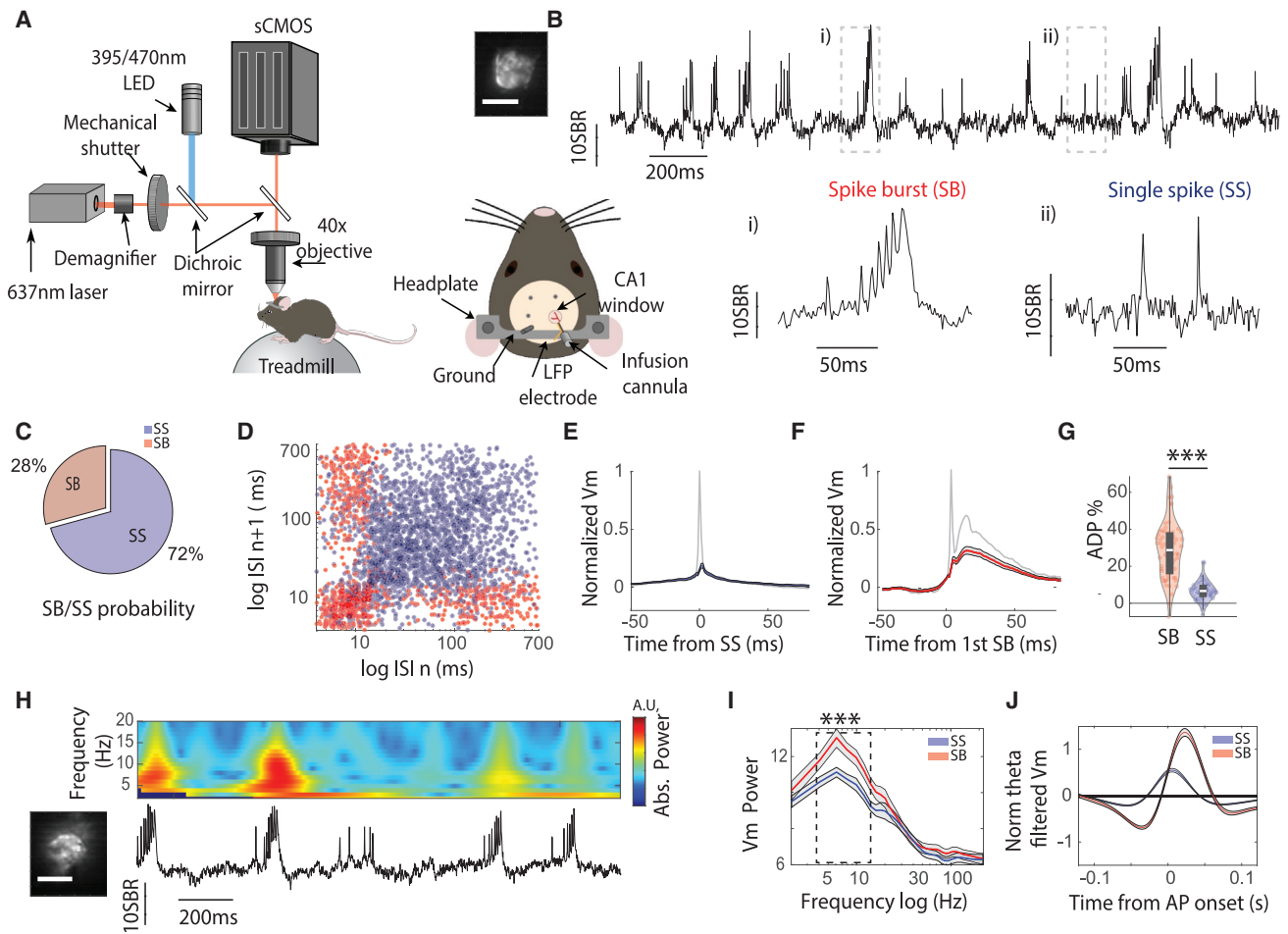
Figure 3. Intracellular SB-associated membrane depolarization contributes to subthreshold Vm theta power

(A) Illustration of SomArchon voltage imaging and animal preparation.

(B) An example 3-second-long SomArchon fluorescence recording at 828 Hz. Left, average SomArchon fluorescence for the neuron recorded. Scale bar, 15 μm. Bottom, zoom-in of the example trace segments indicated by the boxes labeled as (i) and (ii).

(C) Percentage of spikes classified as SBs (all spikes) or SSs (n = 56 neurons).

(D) ISI return map (log scale) for SBs (red) and SSs (blue).

(E and F) SomArchon traces aligned to the peak of SSs (E) or the peak of the first spikes within SB events (F). The gray lines correspond with the mean SomArchon fluorescence. The blue (E) and red lines (F) with the shaded area correspond to SomArchon trace with spikes removed (Vm). Traces are normalized by the averaged spike amplitude.

(G) Quantification of Vm ADP. The ADP was normalized to the pre-spike period (5–25 ms before the spike peak). ADP is stronger in SB than SS (p < 1 × 10^{-20}, df = 56).

(H) An example neuron's SomArchon trace with the corresponding Vm wavelet power spectrum on top. Left, Average SomArchon fluorescence at the spike peak for the neuron shown. Scale bar, 15 μm.

(I) Vm spectral power aligned to SSs (blue) and the first spikes within SB events (red). Vm power at theta frequencies (3–12 Hz, indicated by the box) is greater for SBs than SSs (p = 9.13 × 10^{-8}, df = 43).

(J) Theta-filtered Vm aligned to spikes for either SSs (blue) or the first spikes within SB events (red). All statistics are two-sided one-sample t tests. ***p < 0.001.

(median ± standard deviation; n = 56 neurons) of all recorded spikes were SBs (Figure 3C). The ISI return maps revealed that SBs had a population-averaged intra-burst interval of 8.4 ± 1.9 ms (mean ± standard deviation; n = 56 neurons), consistent with CA1 patch-clamp recordings[3] (Figure 3D).

Another feature of intracellularly recorded complex spikes is the widened action potential waveforms.[33] To characterize the shape of action potentials of SSs and SBs, we performed ultra-fast voltage imaging at 5–10 kHz. We quantified the full width at half maximum (FWHM) amplitude of each action potential and

found that FWHM gradually widened for action potentials within an SB (Figures S4A–S4C), increasing from 0.95 ms (first spike) to 2 ms (fifth spike or more). This increase in FWHM was accompanied with a decrease in action potential amplitude (Figure S4D), again similar to prior patch-clamp observations,[3] and thus further confirmed that SomArchon imaging has sufficient sensitivity to capture individual spikes within SBs.

Compared with SSs, the first spike within an SB was followed by a substantial Vm ADP (see STAR Methods) (peak amplitude, 28.1% ± 1.8% of spike peak, median ± standard deviation;
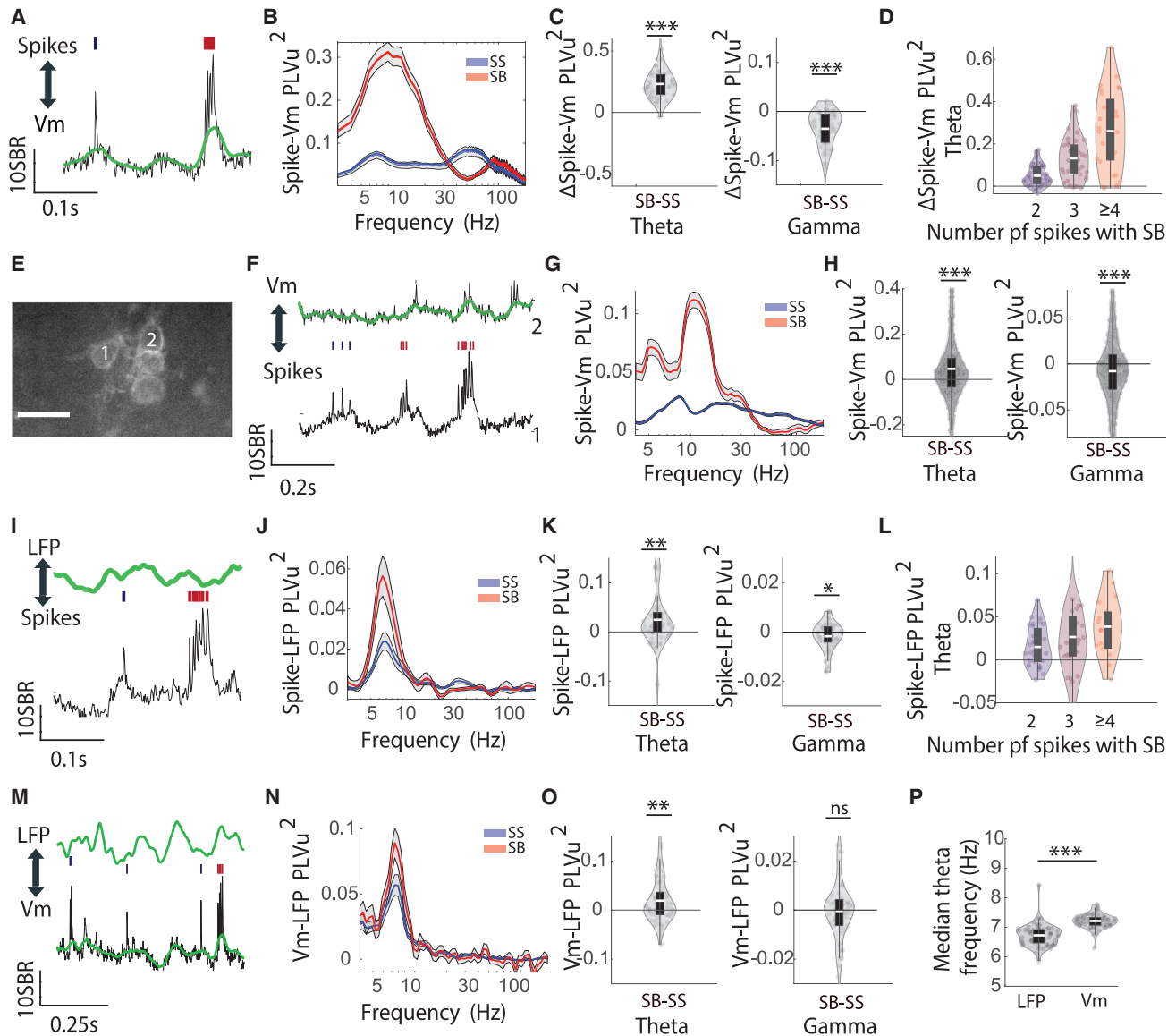
Figure 4. SSs and SBs exhibit distinct phase relationship to cellular Vm and network LFP theta and gamma oscillations

(A) Example SomArchon trace containing both SSs (blue) and SBs (red). The green line corresponds to the theta frequency (3–12 Hz)-filtered Vm trace.

(B) Population $PLVu^2$ of SBs (red) and SSs (blue) to Vm across frequencies (n = 52 neurons). Solid lines correspond to the mean and shaded areas are the standard error of mean.

(C) The difference in population $PLVu^2$ of SBs and SSs to Vm theta and gamma (30–90 Hz). Spike-Vm theta $PLVu^2$ for SBs is greater than for SSs (one-sample t test, p = 1×10^{-20}, df = 51). Spike-Vm gamma $PLVu^2$ for SSs is greater than SBs (one-sample t test, p = 1.4×10^{-7}, df = 51).

(D) Quantification of spike-Vm theta $PLVu^2$ for SB events containing an increasing number of spikes (linear regression, $r^2 = 0.36$, p = 1×10^{-20}; n = 126 SB events concatenated across neurons).

(E–H) Multi-neuron SomArchon recordings using patterned illumination voltage imaging. (E). Example field of view showing GFP fluorescence from simultaneously recorded neurons expressing SomArchon-GFP. Scale bar, 30 μm. (F) Example SomArchon traces from neuron 1 (bottom) and 2 (top) labeled in (E) Spikes in neuron 1 are marked as SBs (red ticks) and SSs (blue ticks). Vm of neuron 2 are highlighted by the green trace. (G) Population $PLVu^2$ of SSs or SBs from one neuron to Vm of another simultaneously recorded neuron. (H) The difference of SB and SS Spike-Vm $PLVu^2$ at theta and gamma frequencies. SBs show stronger theta $PLVu^2$ than SSs (independent t test, p < 1×10^{-20}, df = 1025 spikes, only neurons containing >10 SB and >10 SS were included). SSs exhibit stronger gamma $PLVu^2$ than SB (independent t test, p = 2.3×10^{-8}, df = 1025).

(I–L) Same as (A)–(D), but for spike timing relative to simultaneously recorded LFPs. (K) Spike-LFP theta $PLVu^2$ for SBs is greater than SSs (one-sample t test, p = 0.0037, df = 51). Spike-LFP gamma $PLVu^2$ for SSs is greater than SBs (paired t test, p = 1.8×10^{-3}, df = 51). (L) Spike-LFP theta $PLVu^2$ is significantly higher for SB events containing more spikes (linear regression, $r^2 = 0.05$, p = 0.021; n = 126 SB events).

(legend continued on next page)

n = 56), in sharp contrast to the transient and small ADP (5.6% ± 0.8% of spike peak) after SS (Figures 3E–3G). Further, Vm was significantly hyperpolarized within 100 ms before SBs compared with SSs, which was accompanied by a decreased spike rate (Figures S5A–S5D), in line with a previous patch-clamp study in anesthetized animals.[2] Because the ADP associated with SB occurred on the theta frequency timescale (50–100 ms) (Figure 3D), we next explored the relationship between ADP and Vm spectral power (Figure 3H). We found that SB was associated with a stronger increase in Vm power at theta frequencies (3–12 Hz) than SS (Figures 3I and 3J). Together, these results demonstrate that SB is accompanied by prominent, long-lasting Vm ADP that leads to significantly stronger Vm theta power than SS.

SBs and SSs exhibit distinct temporal relationships to cellular Vm oscillation phase at theta versus gamma frequencies

To investigate how Vm theta power organizes spike timing, we computed the phase locking (PLVu[2]) of each spike within SB or SS relative to Vm theta phase for each neuron (Figure 4A). We observed that SBs exhibited significantly greater spike-Vm PLVu[2] at theta frequencies than SSs, demonstrating that spikes within SBs occur at a more consistent phase of the Vm theta cycle than SSs (Figures 4B and 4C). This result was also observed when we considered only the first spikes within SBs (Figures S1E and S1F), which occurred earlier in the theta cycle than SSs (Figures S5E and S5F). Further, the spike-Vm PLVu[2] at theta frequencies increased linearly with the number of spikes within an SB event (Figure 4D). Thus, not only is SB spike timing preferentially organized by Vm theta phase, but the timing relationship is tighter for more prominent SB events containing a greater number of spikes.

Interestingly, even though SSs exhibited weaker PLVu[2] to Vm theta, SSs showed stronger PLVu[2] at Vm gamma frequencies (30–90 Hz) than SBs (all spikes) (Figures 4B and 4C), even if only the first SB spike was considered (Figures S1E and S1F). We further noted that SBs exhibited stronger PLVu[2] in the high gamma frequency range (100–150 Hz), which likely arose from the short ISI between spikes within SBs. Finally, the same SB phase locking preference for Vm theta was obtained when SBs were identified using ISI alone as with extracellular recordings (Figures S6A–S6C), while SSs exhibited an additional locking preference to Vm gamma.

Cellular voltage imaging analysis reveals that SBs and SSs are coordinated between nearby neurons and regulated by theta versus gamma network rhythms

To directly determine whether the observed spike-Vm phase relationship reflects local network coordination among CA1 neurons, we examined how the Vm of one neuron relates to SSs and SBs from nearby neurons. Specifically, we imaged multiple CA1 neurons simultaneously using a patterned illumination system designed for larger-scale voltage imaging[34] and computed spike-Vm PLVu[2] using spikes of one neuron to the Vm of another nearby neuron (Figures 4E and 4F). We found that SBs exhibited stronger spike-Vm PLVu[2] in the theta range across neurons pairs than SSs, whereas SSs showed additional spike-Vm PLVu[2] in the gamma range (Figures 4G and 4H). These results were replicated when we limited our analysis to neuron pairs being >100 μm apart (Figures S6G–S6I). Thus, distinct Vm rhythms are preferentially linked to SBs and SSs of nearby CA1 neurons, suggesting that SBs and SSs are differentially coordinated locally by theta and gamma network rhythms.

We next examined how the timing of SSs and SBs in individual CA1 neurons recorded with SomArchon imaging relates to the phase of simultaneously recorded hippocampal LFPs (Figure 4I). We found that SBs had stronger PLVu[2] at LFP theta frequencies compared with SSs (Figures 4J and 4K), and PLVu[2] was stronger for SBs containing a greater number of spikes (Figure 4L), similar to that observed with extracellularly recorded spikes in navigating rats. Also consistent, SSs exhibited stronger phase locking at LFP gamma than SBs (Figures 4J and 4K). The fact that SBs exhibited stronger phase locking to both Vm and LFP theta suggests a potential relationship between Vm and LFP theta. Indeed, we found significantly stronger Vm-LFP theta PLVu[2] around SBs than around SSs (Figures 4M–4O).

As LFPs reflect the collective transmembrane currents within a large network, including local and distant circuits, Vm theta may have distinct frequency range compared with LFP theta. Being able to directly measure Vm using SomArchon, we can compare the theta rhythmicity between Vm and LFP. We found that Vm theta frequencies are significantly higher than the simultaneously measured LFP theta (Figure 4P), consistent with previous observations[14] and support the hypothesis that this frequency difference could support Vm-LFP phase precession.
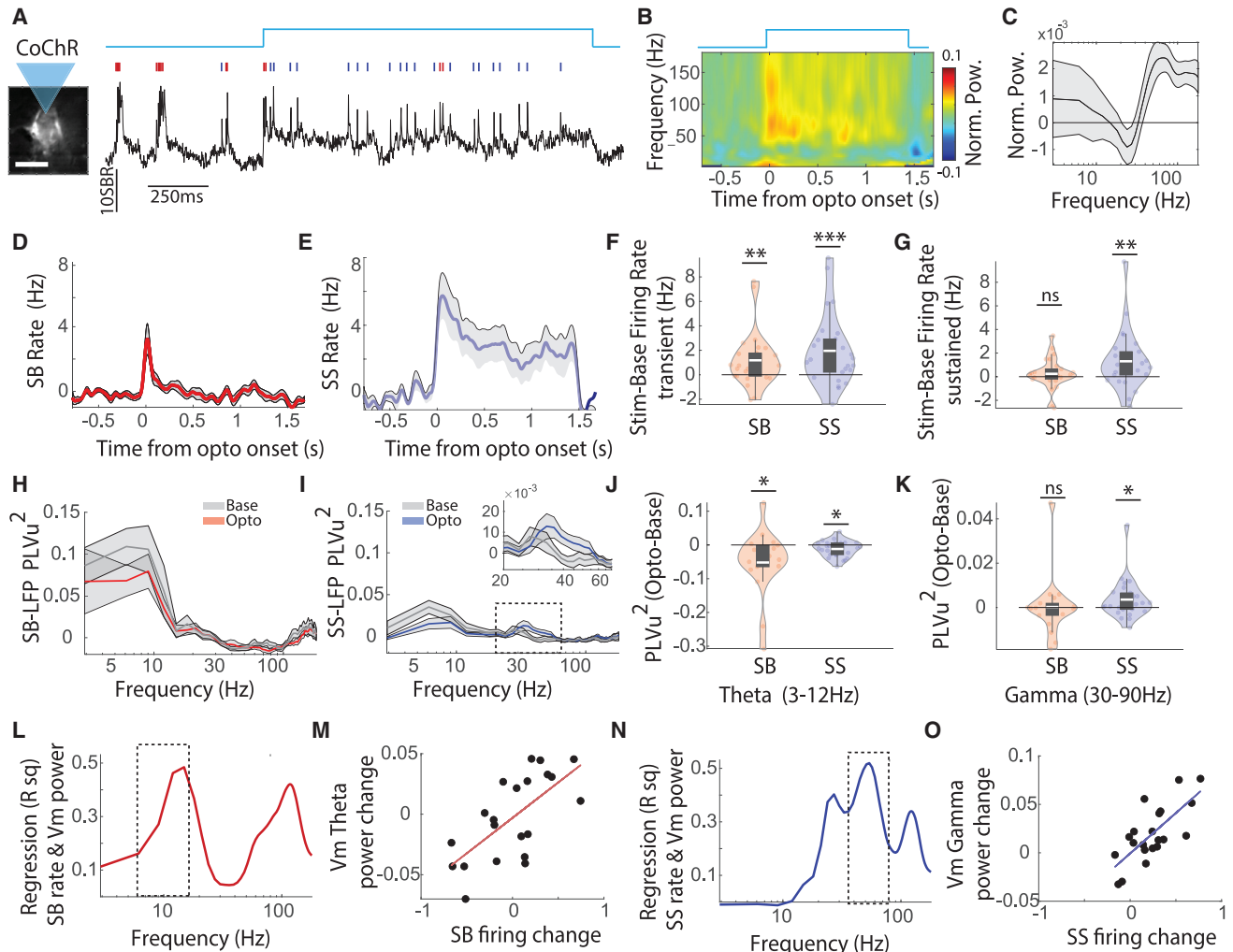
Sustained optogenetic CoChR depolarization confirms that SBs and SSs are differentially coupled to cellular Vm theta versus gamma rhythmicity

The differential coupling of SSs and SBs to Vm and LFP theta and gamma oscillations demonstrates a correlative relationship between the two spiking modes and network coordination. Since action potential initiation is dictated by Vm dynamics, we directly tested the causal relationship between membrane Vm and the probability of SB or SS occurrence. We performed SomArchon voltage imaging while optogenetically depolarizing neurons that co-expressed CoChR using either non-rhythmic or rhythmic optogenetic stimulation.

We first tested how sustained depolarization alters Vm oscillations and spike modes using constant 1.5-s-long blue light to activate CoChR (Figure 5A). We found that population Vm power increased in the broad gamma frequency range (>35 Hz) with a peak centered at 50–55 Hz (Figures 5B

(M–O) Same as (I)–(K) but relating the phase of Vm around SBs or SSs to the phase of simultaneously recorded LFPs. (O). Vm-LFP theta PLVu[2] around SBs is greater than around SSs (paired t test, p = 0.0019, df = 51), but Vm-LFP gamma PLVu[2] is greater for SSs than SBs (one-sample t test, p = 0.9, df = 51).
(P) The median instantaneous theta frequency of simultaneously recorded Vm and LFP. Vm theta frequency is significantly higher than LFP theta frequency (one-sample t test, df = 51, 8.8×10^{-14}).

Figure 5. Sustained optogenetic CoChR depolarization revealed that SBs and SSs are differentially coupled to cellular Vm theta versus gamma power

(A) An example neuron's SomArchon trace before, during and after 1.5-s-long continuous optogenetic activation (blue light illumination pattern on the top). SBs and SSs are marked with red and blue ticks, respectively.

(B) Population Vm wavelet power (n = 26 neurons). Power was first normalized to the 0.5-s baseline before optogenetic (opto) onset, and then averaged across trials.

(C) Stimulation-induced Vm power change calculated as (Vm[stimulation] – Vm[baseline])/(Vm[stimulation] + Vm[baseline]) (n = 26 neurons).

(D and E) Population SB (D) and SS (E) firing rate changes.

(F) Transient change in population firing rate for SBs and SSs within 200 ms of stimulation onset. Both SB (paired t test, p = 0.007, df = 23) and SS (paired t test, p = 1.9×10^{-4}, df = 24) rates increased relative to the baseline.

(G) Sustained change in population firing rate for SBs and SSs during the 0.2–1.5 s after stimulation onset. SSs (paired t test, p = 0.003, df = 24), but not SBs (paired t test, p = 0.96, df = 23), showed a significant increase in firing rate.

(H) SB-LFP $PLVu^2$ across frequencies. Gray line is the $PLVu^2$ values computed from the baseline period (base) and the red line is from the stimulation period (Opto). The shaded area corresponds with the standard error of mean.

(I) Same as (H), but for SSs. The inset is a zoom-in around gamma-frequencies indicated by the box.

(J) Difference of spike-LFP theta $PLVu^2$ between baseline (base) and stimulation (Opto) periods. Spike-Vm theta $PLVu^2$ decreased significantly for both SBs and SSs (one-sample t test, SB, df = 17, p = 0.034; SS, df = 25, p = 0.016).

(K) Same as (J), but for LFP gamma band (30–90 Hz). SS, but not SB, gamma $PLVu^2$ was significantly increased (one-sample t test, SB, df = 17, p = 0.95, SS, df = 25, p = 0.048).

(L) The coefficient of determination (R square) obtained from linear regression between optogenetic-evoked firing rate change of SBs and the change of Vm power across frequencies. Box indicates theta (5–12 Hz).

(M) Scatterplot of optogenetic-evoked SB firing rate change and Vm theta power change. There is a significant positive correlation for SBs (linear regression, $r^2 = 0.45$, p = 0.0009; n = 22), but not for SSs (linear regression, $r^2 = 0.02$, p = 0.57; n = 22).

(N) Same as (L), but for SSs. Box indicates gamma (30–70 Hz).

(O) Scatterplot of optogenetic-evoked SS firing rate change and Vm gamma power change. There is a significant positive correlation for SSs (linear regression, $r^2 = 0.49$, p = 0.0003; n = 22), but not for SBs (linear regression, $r^2 = 0.12$, p = 0.13; n = 22).

and 5C). Optogenetic-induced firing rate changes varied across individual neurons, likely caused by the variation in the efficacy of optogenetics or membrane biophysics across neurons (Figures 5F and 5G). At the population level, spike rates of both SSs and SBs transiently increased at stimulation onset for ~200 ms (Figures 5D–5F), which was followed by a sustained (0.2–1.5 s) increase in the firing rate for SSs, but not SBs (Figure 5G). Sustained optogenetic excitation resulted in a reduction of phase locking to LFP theta for both SSs and SBs (Figure 5H and 5J), but a significant increase in gamma-band phase locking for SSs only (Figures 5I and 5K). As SBs and SSs were differentially related to Vm theta versus gamma, we further explored the relationship between changes in Vm power and firing rate at the individual neuron level. We found that optogenetic-induced changes in SB firing rate correlated with changes in Vm theta power (3–12 Hz) (Figures 5L and 5M), whereas SS firing changes correlated with Vm gamma power (30–90 Hz) (Figures 5N and 5O). Thus, SB and SS generation is driven at least partially by the underlying Vm frequency content.

Patterned optogenetic inputs at 8 and 40 Hz differentially entrain SB and SS outputs

To directly evaluate how Vm rhythmicity influences SBs and SSs, we next pulsed blue light at 8 or 40 Hz. During 8-Hz square-pulse optogenetic stimulation, blue light reliably led to Vm depolarization (Figures 6A and 6B), resulting in a clear 8-Hz Vm spectral band (Figure 6D). The optogenetics-induced Vm depolarization was often accompanied by increased spiking (Figures 6A and 6B). However, only the firing rate of SBs increased significantly relative to baseline (Figure 6C), and SBs showed stronger entrainment to 8-Hz stimulation than SSs (Figure 6E). The 40-Hz stimulation also reliably induced Vm depolarization (Figures 6F and 6G) and entrainment (Figure 6I). While both SBs and SSs showed increases in population firing rate during 40-Hz stimulation, only SSs increased significantly (Figure 6H). In contrast with the 8-Hz stimulation, the 40-Hz stimulation led to significantly stronger entrainment of SSs than SBs (Figure 6J). Together, these findings provide direct causal evidence that Vm theta and gamma rhythmicity determine SS and SB occurrence and organize the timing of SSs and SBs.

Minimal biophysical bursting neuron models capture the distinct Vm rhythmicity preference of SSs and SBs

To explore the biophysical mechanisms of the observed Vm frequency preference of SBs and SSs, we first implemented a previously established minimal two-compartment biophysical model[12,42] of hippocampal pyramidal cells[9,13,43] (Figure 7A), which includes dendritic SB-generating persistent sodium (NaP) and slow potassium (KS) currents (STAR Methods). We chose conductance values for NaP and KS that generate intermittent SBs and SSs.[9] As NaP and KS contribute to subthreshold resonance[44–47] at theta frequencies,[48–50] we first confirmed that the model exhibited Vm theta resonance, peaking at ~4 Hz, using a chirp (increasing frequency) dendritic subthreshold input (Figures 7C and 7D).

We then tested whether SBs and SSs exhibited differential phase locking to theta and gamma inputs as observed experimentally. We initiated the model with a dendritic input containing

theta and gamma rhythmicity and Gaussian white noise, along with a constant depolarizing input at the soma/axon compartment. Similar to the experimental results, SBs showed preferential phase locking to theta rhythmic inputs (all SBs, Figure 7E) with a similar earlier theta phase preference compared with SSs (Figures S5I and S5J). SSs showed prominent phase locking to gamma inputs (Figure 7E) but weaker phase locking to theta inputs compared with SBs. Furthermore, SB theta locking increased with a growing number of spikes within an SB event (Figure 7F). Finally, to better capture the Vm frequency preference of SBs and SSs, we used non-structured Gaussian white noise dendritic inputs (flat frequency spectrum). We found that SBs (Figures 7G and 7H) exhibited stronger phase locking to theta (~3–12 Hz) inputs than SSs, particularly for SBs with more spikes. In contrast, SSs exhibited stronger phase locking to broader gamma frequency inputs (~25–100 Hz).

Further exploration of SB and SS phase relationship to different input rhythms using a more complex biophysical model of CA1 pyramidal neurons that generates SBs through HCN dendritic currents[48,51,52] yielded similar results (Figures S7A–S7C). Finally, as N-methyl-D-aspartate (NMDA) receptor activation contributes to the generation of CA1 complex SBs[53] and dendritic spikes,[53] we added NMDA current into the HCN burst model. While increasing the NMDA synaptic current activation rate enhanced SB probability and decreased SS probability, we found no effect on theta versus gamma entrainment (Figures S7D and S7E), consistent with the slow NMDA channel kinetics.[54]

Based on the experimental observation of ramping Vm depolarization in CA1 neurons during place field traversals[14] and modeling studies[13,55] showing that ramping dendritic input leads to linear phase precession,[55] we simulated place field inputs as an asymmetric ramping dendritic input of 1 s in total duration (700 ms ramping up and 300 ms ramping down). As expected, we observed the precession of spike timing relative to theta phase (Figure 7I), similar to that observed in our tetrode recordings in navigating rats. Furthermore, SBs carried more spatial information of the place field dendritic inputs (Figure 7J), also consistent with our observations (Figure 2). SBs occurred preferentially on the rising slope of the place field dendritic input as reflected in the shifted COM relative to SSs (Figure 7K), again similar to our experimental findings of the preferred SB occurrence when animals first entered the place field (Figure 2). Finally, when separating SB and SS during the calculation of spike phase precession to theta-rhythmic place field dendritic inputs, we found that SBs exhibited stronger phase precession quantified as circular-linear correlation (Figure 7I), as observed in our navigating rats (Figure 2).

Together, the two minimal biophysical CA1 SB models captured the key features of the experimentally observed SB and SS phase-locking preferences, demonstrating that the intrinsic biophysical properties underlying SB and SS generation are sufficient to support the differential spiking response to theta versus gamma rhythmic inputs. Further, the intrinsic membrane properties underlying SB production can mediate distinct place field coding of SBs and SSs during spatial navigation. Thus, both our computational models and experimental observations suggest that SBs and SSs represent two spiking output modes
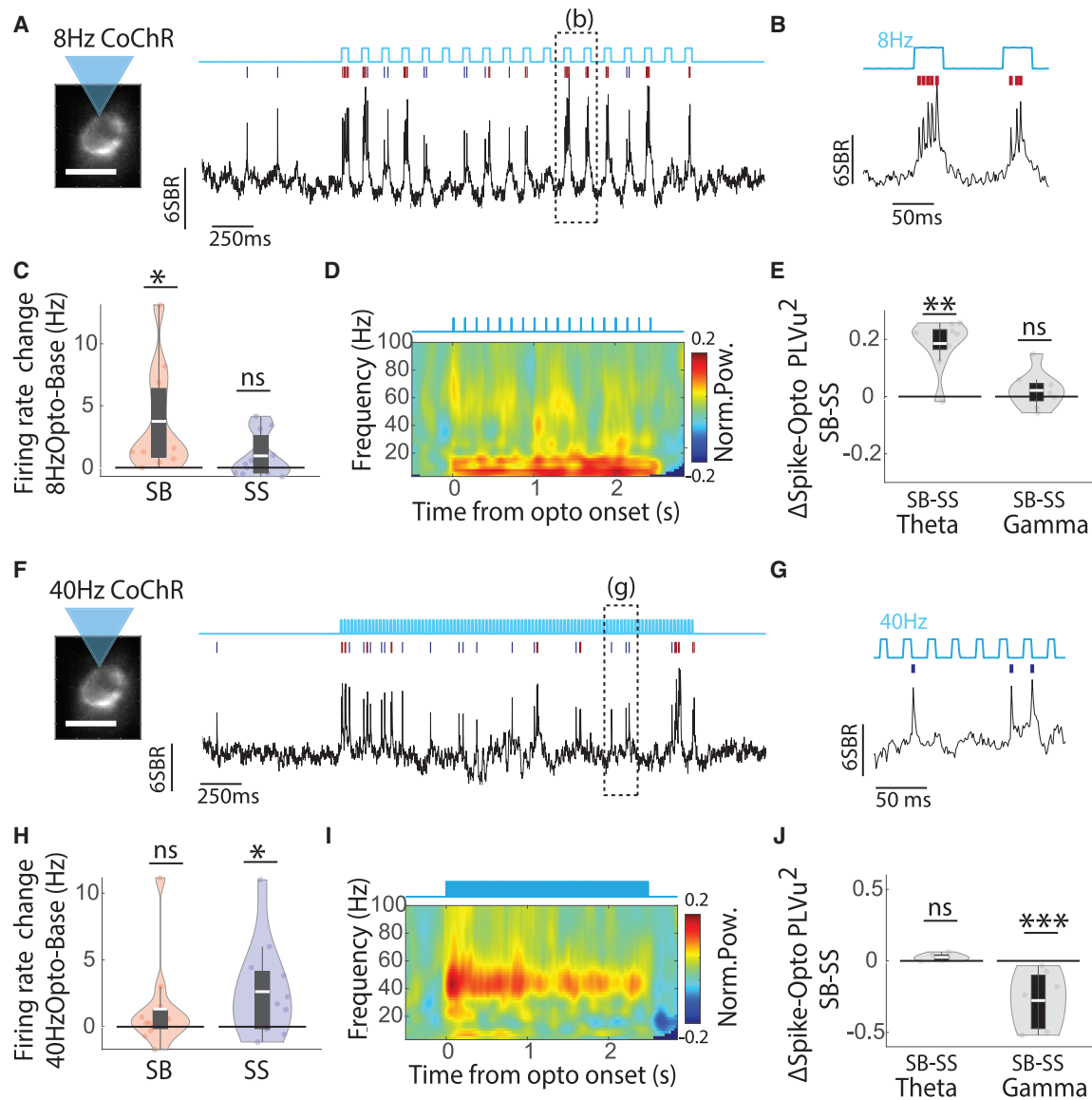
Figure 6. Optogenetic 8- and 40-Hz pulsed depolarization inputs differentially entrain SB and SS outputs

(A) An example SomArchon trace before, during and after 1.5-s-long, 8-Hz pulsed optogenetic activation (blue light illumination pattern on the top). SBs and SSs are marked with red and blue ticks, respectively. Left, Average SomArchon fluorescence at spike peak for the example neuron shown. Scale bar, 15 μm. Dashed box indicates the zoom-in shown in (B).

(B) Zoom-in view of the example trace shown in (A).

(C) Optogenetic-induced firing rate changes for SBs (red) and SSs (blue), calculated as the rate during stimulation minus the rate during baseline (0.5 s before stimulation onset). SBs are significantly enhanced by 8-Hz stimulation (one-sample t test, p = 0.014, df = 10), but not SSs (one-sample t test, p = 0.10, df = 10).

(D) Population Vm wavelet spectral power during 8-Hz stimulation. Power for each neuron was first normalized to the baseline for each trial, and then averaged across trials.

(E) Quantification of spike $PLVu^2$ to 8-Hz stimulation pulse patterns for SBs (red) and SSs (blue). $PLVu^2$ for SBs is significantly higher than for SSs at theta frequencies (one-sample t test, p = 3.23×10^{-4}, df = 8), and no difference at gamma frequencies (one-sample t test, p = 0.59, df = 8).

(F and G) Same as (A) and (B) but for an example trial of the same neuron upon 40-Hz stimulation.

(H) Same as (C) but for 40-Hz stimulation. SS firing rate is significantly higher during the stimulation period than the baseline (one-sample t test, p = 0.022, df = 11), but not SB firing rate (one-sample t test, p = 0.19, df = 11).

(I). Same as (D) but for 40-Hz stimulation.

(J) Quantification of spike-Vm $PLVu^2$ to 40-Hz stimulation pulse pattern. SS $PLVu^2$ is significantly stronger than SB at gamma frequencies (one-sample t test, SS, p = 0.012, df = 6), but no difference at theta (one-sample t test, SB, p = 0.096, df = 6). Opto, optogenetic stimulation.
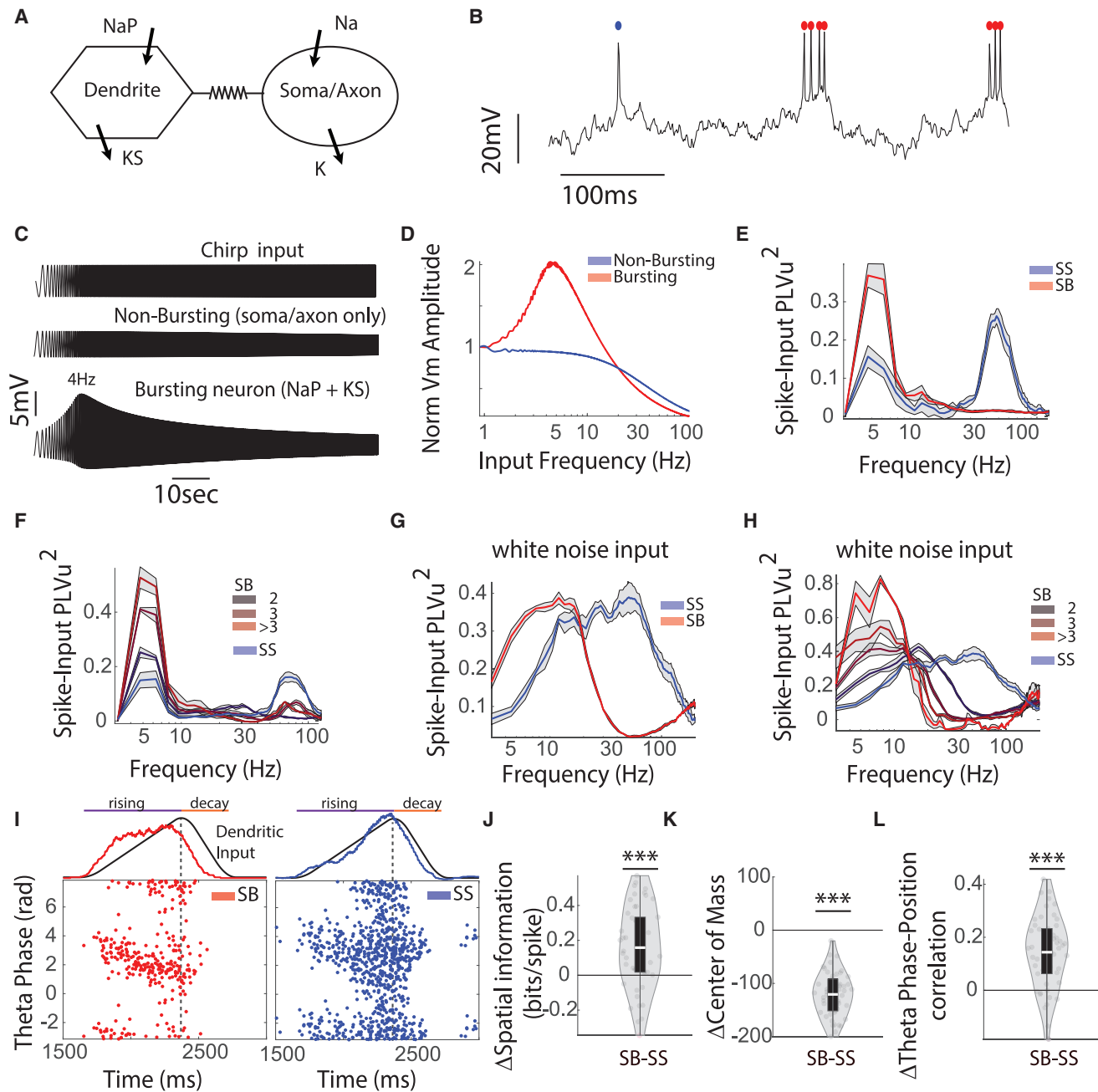
Figure 7. A biophysical CA1 neuron model recapitulates the distinct Vm rhythmicity preference and coding of SSs and SBs

(A) Schematic model of the two-compartment Hodgkin-Huxley bursting neuron model.

(B) Example output membrane voltage trace of the model neuron. SBs and SSs are marked by red and blue ticks, respectively.

(C) The subthreshold Vm response of the modeled non-bursting neuron (middle) and bursting neuron (bottom) in response to chirp inputs of increasing frequency from 0.2 to 20 Hz (top).

(D) Normalized Vm amplitude over chirp input frequencies. Vm amplitude is normalized to the Vm amplitude at 1Hz.

(E) $PLVu^2$ of spikes to dendritic inputs across frequencies. All SB spikes are used.

(F) Same as (E), but computing $PLVu^2$ for SSs and SBs containing an increasing number of spikes (2, 3, and >3 spikes). Only the first SB spikes were used for $PLVu^2$ calculation.

(G and H) Same as (E) and (F), but with the dendritic compartment receiving only white noise input.

(I) The spike timing of a simulated neuron to input theta phase at different positions of the neuron's place field. An asymmetric excitatory input (black line, top) is used to model the place field input. The average firing rate for SBs (red line, top) or SSs (blue line, top) is overlaid over the input. Each dot indicates a spike. The dashed black line indicates the center of the place field.

(legend continued on next page)

that are differentially regulated by theta and gamma rhythmic inputs and thereby code different information during behavior.

DISCUSSION

Using the recently developed SomArchon-based single-cell voltage imaging,[31,34,35] optogenetics, and conventional extracellular recordings, we studied the relationship of SBs and SSs to network-level LFP rhythms and cellular-level membrane voltage dynamics in CA1. We found that SBs and SSs co-exist in most neurons analyzed in rats during spatial navigation and in awake head-fixed mice in both our own voltage imaging dataset and in the Allen Brain Institute dataset. SBs and SSs were preferentially accompanied by network-level LFP and cellular-level Vm theta versus gamma rhythms, and optogenetic Vm depolarization experiments revealed a causal link between Vm theta and gamma rhythmicity in the preferential generation of SBs versus SSs. Furthermore, the SB firing rate and phase coding carried different spatial information than SS during spatial navigation. Finally, minimal biophysical models of CA1 spike bursting neurons recapitulated our experimental findings, suggesting that intrinsic cellular biophysical dynamics alone are sufficient to support the observed coupling of SBs and SSs to Vm theta and gamma rhythmicity and the place field coding properties during spatial navigation. These results provide direct evidence that SBs and SSs are distinct spiking outputs of hippocampal CA1 neurons that differentially transmit theta versus gamma circuit rhythmicity during behavior.

We observed consistent SB and SS coupling preference to LFP theta and gamma across several datasets, including extracellular tetrode recording data in navigating rats, extracellular Neuropixels recording data in head-fixed mice provided by the Allen Brain Institute, and single-cell voltage imaging data in head-fixed, freely locomoting mice. Thus, SB- and SS-mediated circuit rhythm coding is a robust and universal feature of CA1. While CA1 neurons' spikes are correlated with both Vm and LFP theta, Vm theta can decorrelate from LFP theta during place field traversals.[14,21,24,25,56] For example, Harvey et al. observed that while LFP theta power remained constant during place field activation, cellular Vm theta power was modulated.[14] We found that SBs play a critical role in Vm theta dynamics, and Vm theta has a higher frequency than LFP theta, supporting the notion that single neurons' subthreshold theta rhythm is less stationary than LFP theta. Further, we found that SBs of one neuron were phase locked to the Vm theta of other nearby neurons, suggesting that CA1 neurons are coordinated locally at theta frequencies, and SBs transmit theta coordinated circuit output. Since pyramidal neurons exhibit little direct connectivity, such coordination is more likely mediated by local interneurons or shared external theta rhythmic inputs from CA3 or medial septum.

In contrast to the prominent theta frequency phase locking of SBs, SSs exhibited stronger phase locking to Vm and LFP gamma. This effect remains when considering only the first spike within an SB, suggesting that SB onset is also less phase locked than SS. The gamma range of SS phase locking occurred at slow to middle gamma ranges (30–100 Hz).[27,28] Since SB is associated with strong dendritic and somatic membrane depolarization that leads to the ballistic generation of high-frequency spikes, leading to multiple spikes per gamma cycle, the occurrence of SB likely prevents reliable entrainment of SB by gamma-rhythmic inputs.

The computational role of SB and SS in spatial memory

Hippocampal theta and gamma rhythms are thought to carry behavioral information during spatial navigation and memory,[21–25] because of their distinct generation[21,29] and propagation mechanisms.[26,40] Theta phase has been shown to carry information about spatial position[24,57] and to provide a temporal window for cognitive state-dependent[25,58] cross-area communication.[28,40] In particular, spike-LFP theta phase precession over spatial position has been intensively studied over the years.[14,24,40] We found that SBs exhibited more precise theta phase precession than SSs. Further, theta phase precession was particularly predictive of spatial position in the first half of the place field, when SB occurrence was dominant, but less precise in the second half of the place field when SS dominated. This is in line with the reported reduced precision of phase precession in the late phase of place field traversal.[24] Additionally, SBs were strongly related to sub-threshold membrane voltage theta rhythms, which is likely due to the large ADPs associated with SBs. Hippocampal SBs, governed by membrane ionic currents known to have theta frequency resonance,[45,50,55] thus seem to be optimal to support theta-rhythmic computations during spatial navigation and memory.

Gamma rhythms are prominent in the hippocampus and associated structures. Gamma power occurs at different frequency bands across distinct brain areas that project to CA1.[28,59] Slow gamma (~30–40 Hz) dominates CA3-CA1 projection, whereas mid gamma (~50–100 Hz) dominates entorhinal-CA1 projection. High gamma (>100 Hz) seems to be locally generated within CA1. The function of gamma rhythms in the hippocampus is not well understood, but it is generally thought that gamma rhythms enable efficient pathway-specific cross-area communication.[26,60] Our observations illustrate that gamma frequencies preferentially entrain SSs, suggesting that pathway-specific gamma-band communication[26,30,60] is primarily carried by SSs. Further, we found that SSs occurred preferentially in the late phase of place field traversals with prominent phase locking at mid-gamma range, as shown previously.[59]

It has been shown that spikes can be misaligned[61–63] relative to the peak firing rate within the place field, for example, because of an animal's movement direction. Spikes that precede the

---

(J) The difference in SB and SS spatial information metrics calculated as bits per spike (df = 49, p = 1.50 × 10⁻⁵).

(K) The difference in COM calculated using neurons' SSs and SBs (df = 49, p < 1 × 10⁻²⁰).

(L) The difference in circular-linear correlation values between spike phase relative to input theta (8 Hz) and spatial position modeled by asymmetric excitatory input shown in (I). SBs show stronger theta phase correlations with spatial position than SSs (df = 49, p = 8.67 × 10⁻⁶). All statistics are two-sided one-sample t tests. ***p < 0.005.

place field center are thought to provide prospective coding, whereas spikes after the place field center provide retrospective coding, and thus mediating encoding and retrieval processes, respectively. Here, we found that SBs often preceded the peak firing rate within the place field, whereas SSs often followed the peak firing rate, suggesting that SBs and SSs could differentially mediate prospective and retrospective coding. The distinct circuit coding of SB versus SS is at least partially attributed to the preferential production of SBs on the positive slope of incoming input (hysteresis), whereas the firing rate of SSs scales linearly with place field inputs as shown in computational models utilized here and in previous studies.[9]

The biophysical mechanism underlying the frequency-dependent generation of SBs and SSs

SB generation involves specific voltage-dependent membrane currents[15] and dendritic plateau potentials[6,10,16] that require conjunctive dendritic and somatic activation.[16] While some studies suggested that CA1 SBs can occur with somatic membrane channel dynamics alone,[15,64] including NaP currents and KS currents (M currents), other studies have emphasized the important of dendritic dynamics.[6,12,13,16,42,65,66] Our minimal biophysical conductance-based models, which are based on established hippocampal pyramidal models[12,15,43] comprising somatic and dendritic compartments, were sufficient to reproduce most aspects of the experimental data. While the classical sodium and potassium currents underlying action potential generation have a broadband frequency selectivity, the ion channel currents (NaP, KS, or HCN) underlying SB generation exhibit theta resonance. Thus, it is conceivable that inputs at theta frequency, structured or unstructured, could be amplified by the ionic currents underlying theta resonance as well as SBs, which results in tight coupling between theta rhythmic input, Vm theta, and SBs. In contrast, SSs generated predominately by channels with fast kinetics are more sensitive to high-frequency modulations.

In addition to intrinsic biophysical features, it is plausible that rhythmic inputs at theta versus gamma frequencies selectively recruit synaptic currents to further support the rhythmic somatic Vm fluctuations responsible for the production of these two distinct spike outputs. In particular, SBs and SSs might critically rely on the timing of inhibitory synaptic currents that originate from an interplay between interneurons that target the soma versus the dendrites.[10,67] For example, dendritic-targeting oriens-lacunosum moleculare inhibitory cells have theta resonance[46,67,68] and exhibit Vm theta,[5] and might contribute to theta-rhythmic pyramidal SB generation.[52,67] In contrast, soma-targeting parvalbumin (PV) interneurons exhibit gamma resonance[68,69] and might contribute more to gamma-rhythmic SS generation. PV interneurons might have contributed to our observation that 40-Hz optogenetic stimulation particularly enhanced SSs, as fast spiking interneurons show resonance in the gamma frequency range.[69]

It has been suggested that CA1 SB generation depends on strong membrane depolarization after hyperpolarization,[2] while tonic excitation favors SS generation. Consistent with this idea, we observed Vm hyperpolarization and decreased spike proba-

bility before SBs, and tonic optogenetic stimulation led to enhanced SS probability. Further, SBs occurred during the initial part of the place field characterized by ramping excitation,[14] while SSs occurred at the later part of the place field. The SB preference for non-tonic activation dynamics is consistent with its theta-rhythmic preference. Theta rhythms are synchronized across different structures of the hippocampus, including CA3 and EC pathways that activate CA1 neurons in a theta phase-dependent manner.[16,21] Coordinated dendritic and somatic activation of CA1 neurons have been found to support burst generation[10,16,70] and might explain why bursts are strongly theta locked. In contrast, gamma rhythms have been found to be locally generated and occur at variable frequencies across CA1 layers and throughout different structures of the hippocampus,[28] which might, therefore, favor SSs.

Limitations of the study

While separating SB from SS in extracellular studies has been commonly done using ISI thresholding, ISI distribution for individual neurons is often not bimodal, making it a methodological challenge to separate SB and SS using ISI alone. Further development of burst detection algorithms or using techniques capable of resolving cellular membrane voltage, such as patch-clamp or voltage imaging, will be important to distinguish these distinct spike modes with high fidelity.

A previous patch-clamp study[14] demonstrated that sub-threshold theta rhythms and spikes in a small number of CA1 neurons both phase precess to LFP theta during spatial navigation. Our voltage imaging recordings were performed in mice freely locomoting without defined spatial navigation task structures. It will be informative to evaluate how Vm-LFP relationship relates to place field structures in mice navigating a virtual environment using voltage imaging in the future.

STAR★METHODS

Detailed methods are provided in the online version of this paper and include the following:

- KEY RESOURCES TABLE
- RESOURCE AVAILABILITY
  - Lead contact
  - Materials availability
  - Data and code availability
- EXPERIMENTAL MODEL AND SUBJECT DETAILS
- METHOD DETAILS
  - Spatial information and sparsity index
  - Center of mass (COM) calculation
  - NMDA current input incorporated into the h-current bursting model
- QUANTIFICATION AND STATISTICAL ANALYSIS

REFERENCES

1. Ranck, J.B. (1973). Studies on single neurons in dorsal hippocampal formation and septum in unrestrained rats: Part I. Behavioral correlates and firing repertoires. Exp. Neurol. *41*, 462–531.

2. Harris, K.D., Hirase, H., Leinekugel, X., Henze, D.A., and Buzsáki, G. (2001). Temporal Interaction between Single Spikes and Complex Spike Bursts in Hippocampal Pyramidal Cells. Neuron *32*, 141–149.

3. Epsztein, J., Brecht, M., and Lee, A.K. (2011). Intracellular Determinants of Hippocampal CA1 Place and Silent Cell Activity in a Novel Environment. Neuron *70*, 109–120.

4. Csicsvari, J., Hirase, H., Czurko, A., and Buzsáki, G. (1998). Reliability and State Dependence of Pyramidal Cell–Interneuron Synapses in the Hippocampus: an Ensemble Approach in the Behaving Rat. Neuron *21*, 179–189.

5. Adam, Y., Kim, J.J., Lou, S., Zhao, Y., Xie, M.E., Brinks, D., Wu, H., Mostajo-Radji, M.A., Kheifets, S., Parot, V., et al. (2019). Voltage imaging and optogenetics reveal behaviour-dependent changes in hippocampal dynamics. Nature *569*, 413–417.

6. Apostolides, P.F., Milstein, A.D., Grienberger, C., Bittner, K.C., and Magee, J.C. (2016). Axonal Filtering Allows Reliable Output during Dendritic Plateau-Driven Complex Spiking in CA1 Neurons. Neuron *89*, 770–783.

7. Lisman, J.E. (1997). Bursts as a unit of neural information: making unreliable synapses reliable. Trends Neurosci. *20*, 38–43.

8. Kepecs, A., and Lisman, J. (2003). Information encoding and computation with spikes and bursts. Netw. Comput. Neural Syst. *14*, 103–118.

9. Kepecs, A., Wang, X.J., and Lisman, J. (2002). Bursting Neurons Signal Input Slope. J. Neurosci. *22*, 9053–9062.

10. Milstein, A.D., Bloss, E.B., Apostolides, P.F., Vaidya, S.P., Dilly, G.A., Zemelman, B.V., and Magee, J.C. (2015). Inhibitory Gating of Input Comparison in the CA1 Microcircuit. Neuron *87*, 1274–1289.

11. Cohen, J.D., Bolstad, M., and Lee, A.K. (2017). Experience-dependent shaping of hippocampal CA1 intracellular activity in novel and familiar environments. Elife *6*, e23040.

12. Traub, R.D., Wong, R.K., Miles, R., and Michelson, H. (1991). A model of a CA3 hippocampal pyramidal neuron incorporating voltage-clamp data on intrinsic conductances. J. Neurophysiol. *66*, 635–650.

13. Kamondi, A., Acsády, L., Wang, X.-J., and Buzsáki, G. (1998). Theta oscillations in somata and dendrites of hippocampal pyramidal cells in vivo: Activity-dependent phase-precession of action potentials. Hippocampus *8*, 244–261.

14. Harvey, C.D., Collman, F., Dombeck, D.A., and Tank, D.W. (2009). Intracellular dynamics of hippocampal place cells during virtual navigation. Nature *461*, 941–946.

15. Golomb, D., Yue, C., and Yaari, Y. (2006). Contribution of persistent Na+ current and M-type K+ current to somatic bursting in CA1 pyramidal cells: Combined experimental and modeling study. J. Neurophysiol. *96*, 1912–1926.

16. Bittner, K.C., Grienberger, C., Vaidya, S.P., Milstein, A.D., Macklin, J.J., Suh, J., Tonegawa, S., and Magee, J.C. (2015). Conjunctive input processing drives feature selectivity in hippocampal CA1 neurons. Nat. Neurosci. *18*, 1133–1142.

17. Bittner, K.C., Milstein, A.D., Grienberger, C., Romani, S., and Magee, J.C. (2017). Behavioral time scale synaptic plasticity underlies CA1 place fields. Science *357*, 1033–1036.

18. Wong, R.K., Traub, R.D., and Miles, R. (1986). Cellular basis of neuronal synchrony in epilepsy. Adv. Neurol. *44*, 583–592.

19. Sanabria, E.R., Su, H., and Yaari, Y. (2001). Initiation of network bursts by Ca $^{2+}$ -dependent intrinsic bursting in the rat pilocarpine model of temporal lobe epilepsy. J. Physiol. *532*, 205–216.

20. Tryba, A.K., Kaczorowski, C.C., Ben-Mabrouk, F., Elsen, F.P., Lew, S.M., and Marcuccilli, C.J. (2011). Rhythmic intrinsic bursting neurons in human neocortex obtained from pediatric patients with epilepsy. Eur. J. Neurosci. *34*, 31–44.

21. Buzsáki, G. (2002). Theta oscillations in the hippocampus. Neuron *33*, 325–340.

22. Mizuseki, K., Sirota, A., Pastalkova, E., and Buzsáki, G. (2009). Theta Oscillations Provide Temporal Windows for Local Circuit Computation in the Entorhinal-Hippocampal Loop. Neuron *64*, 267–280.

23. McFarland, W.L., Teitelbaum, H., and Hedges, E.K. (1975). Relationship between hippocampal theta activity and running speed in the rat. J. Comp. Physiol. Psychol. *88*, 324–328.

24. Skaggs, W.E., McNaughton, B.L., Wilson, M.A., and Barnes, C.A. (1996). Theta phase precession in hippocampal neuronal populations and the compression of temporal sequences. Hippocampus *6*, 149–172.

25. Hasselmo, M.E. (2005). What Is the Function of Hippocampal Theta Rhythm? - Linking Bahavioral Data to Phasic Properties of Field Potential and Unit Recording Data (Hippocampus).

26. Fernández-Ruiz, A., Oliva, A., Soula, M., Rocha-Almeida, F., Nagy, G.A., Martin-Vazquez, G., and Buzsáki, G. (2021). Gamma rhythm communication between entorhinal cortex and dentate gyrus neuronal assemblies. Science *80*, 372.

27. Colgin, L.L., Denninger, T., Fyhn, M., Hafting, T., Bonnevie, T., Jensen, O., Moser, M.-B., and Moser, E.I. (2009). Frequency of gamma oscillations routes flow of information in the hippocampus. Nature *462*, 353–357.

28. Schomburg, E.W., Fernández-Ruiz, A., Mizuseki, K., Berényi, A., Anastassiou, C.A., Koch, C., and Buzsáki, G. (2014). Theta Phase Segregation of Input-Specific Gamma Patterns in Entorhinal-Hippocampal Networks. Neuron *84*, 470–485.

29. Traub, R.D., Whittington, M.A., Colling, S.B., Buzsáki, G., and Jefferys, J.G. (1996). Analysis of gamma rhythms in the rat hippocampus in vitro and in vivo. J. Physiol. *493*, 471–484.

30. Buzsáki, G., and Wang, X.-J. (2012). Mechanisms of gamma oscillations. Annu. Rev. Neurosci. *35*, 203–225.

31. Piatkevich, K.D., Bensussen, S., Tseng, H.A., Shroff, S.N., Lopez-Huerta, V.G., Park, D., Jung, E.E., Shemesh, O.A., Straub, C., Gritton, H.J., et al.

(2019). Population imaging of neural activity in awake behaving mice. Nature *574*, 413–417.

32. Lowet, E., Kondabolu, K., Zhou, S., Mount, R.A., Wang, Y., Ravasio, C.R., and Han, X. (2022). Deep brain stimulation creates informational lesion through membrane depolarization in mouse hippocampus. Nat. Commun. *13*, 7709.

33. Lowet, E., Mertz, J., Xiao, S., and Han, X. (2021). Ultrafast Voltage Imaging of Single Neurons at Ten Kilohertz in Behaving Mice. Front. Opt. + Laser Sci. *2021*. Pap. FM5E.1, FM5E.1.

34. Xiao, S., Lowet, E., Gritton, H.J., Fabris, P., Wang, Y., Sherman, J., Mount, R.A., Tseng, H.A., Man, H.-Y., Straub, C., et al. (2021). Large-scale voltage imaging in behaving mice using targeted illumination. iScience *24*, 103263.

35. Fan, L.Z., Kheifets, S., Böhm, U.L., Wu, H., Piatkevich, K.D., Xie, M.E., Parot, V., Ha, Y., Evans, K.E., Boyden, E.S., et al. (2020). All-Optical Electrophysiology Reveals the Role of Lateral Inhibition in Sensory Processing in Cortical Layer 1. Cell *180*, 521–535.e18.

36. Moser, E.I., Kropff, E., and Moser, M.-B. (2008). Place Cells, Grid Cells, and the Brain's Spatial Representation System. Annu. Rev. Neurosci. *31*, 69–89.

37. Buzsáki, G. (2006). Rhythms of the Brain (Oxford University Press).

38. Best, P.J., White, A.M., and Minai, A. (2001). Spatial Processing in the Brain: The Activity of Hippocampal Place Cells. Annu. Rev. Neurosci. *24*, 459–486.

39. Mizuseki, K., Diba, K., Pastalkova, E., and Buzsáki, G. (2011). Hippocampal CA1 pyramidal cells form functionally distinct sublayers. Nat. Neurosci. *14*, 1174–1181.

40. Mizuseki, K., Royer, S., Diba, K., and Buzsáki, G. (2012). Activity Dynamics and Behavioral Correlates of CA3 and CA1 Hippocampal Pyramidal Neurons. Hippocampus *22*, 1659–1680.

41. Gourévitch, B., and Eggermont, J.J. (2007). A nonparametric approach for detection of bursts in spike trains. J. Neurosci. Methods *160*, 349–358.

42. Pinsky, P.F., and Rinzel, J. (1994). Intrinsic and network rhythmogenesis in a reduced traub model for CA3 neurons. J. Comput. Neurosci. *1*, 39–60.

43. Kepecs, A., and Wang, X.J. (2000). Analysis of complex bursting in cortical pyramidal neuron models. Neurocomputing *32–33*, 181–187.

44. Hu, H., Vervaeke, K., Graham, L.J., and Storm, J.F. (2009). Complementary theta resonance filtering by two spatially segregated mechanisms in CA1 hippocampal pyramidal neurons. J. Neurosci. *29*, 14472–14483.

45. Rotstein, H.G., and Nadim, F. (2014). Frequency preference in two-dimensional neural models: A linear analysis of the interaction between resonant and amplifying currents. J. Comput. Neurosci. *37*, 9–28.

46. Rotstein, H.G. (2015). Subthreshold amplitude and phase resonance in models of quadratic type: Nonlinear effects generated by the interplay of resonant and amplifying currents. J. Comput. Neurosci. *38*, 325–354.

47. Hutcheon, B., and Yarom, Y. (2000). Resonance, oscillation and the intrinsic frequency preferences of neurons. Trends Neurosci. *23*, 216–222.

48. Hu, H., Vervaeke, K., and Storm, J.F. (2002). Two forms of electrical resonance at theta frequencies, generated by M-current, h-current and persistent Na+ current in rat hippocampal pyramidal cells. J. Physiol. *545*, 783–805.

49. Giocomo, L.M., Zilli, E.A., Fransén, E., and Hasselmo, M.E. (2007). Temporal frequency of subthreshold oscillations scales with entorhinal grid cell field spacing. Science *80*.

50. Leung, L.S., and Yu, H.-W. (1998). Theta-Frequency Resonance in Hippocampal CA1 Neurons In Vitro Demonstrated by Sinusoidal Current Injection. J. Neurophysiol. *79*, 1592–1596.

51. Stark, E., Eichler, R., Roux, L., Fujisawa, S., Rotstein, H.G., and Buzsáki, G. (2013). Inhibition-Induced theta resonance in cortical circuits. Neuron *80*, 1263–1276.

52. Sinha, M., and Narayanan, R. (2015). HCN channels enhance spike phase coherence and regulate the phase of spikes and LFPs in the theta-frequency range. Proc. Natl. Acad. Sci. USA *112*, E2207–E2216.

53. Grienberger, C., Chen, X., and Konnerth, A. (2014). NMDA receptor-dependent multidendrite Ca^{2+} spikes required for hippocampal burst firing invivo. Neuron *81*, 1274–1281.

54. Ermentrout, G.B., and Terman, D.H. (2010). Mathematical Foundations of Neuroscience (Springer).

55. Leung, L.S. (2011). A model of intracellular theta phase precession dependent on intrinsic subthreshold membrane currents. J. Neurosci. *31*, 12282–12296.

56. Burgess, N., and O'Keefe, J. (2011). Models of place and grid cell firing and theta rhythmicity. Curr. Opin. Neurobiol. *21*, 734–744.

57. Siegle, J.H., and Wilson, M.A. (2014). Enhancement of Encoding and Retrieval Functions through Theta Phase-specific Manipulation of hippocampus. Elife. 2014.

58. Hasselmo, M.E., and Stern, C.E. (2014). Theta Rhythm and the Encoding and Retrieval of Space and Time (Neuroimage).

59. Lasztóczi, B., and Klausberger, T. (2016). Hippocampal Place Cells Couple to Three Different Gamma Oscillations during Place Field Traversal. Neuron *91*, 34–40.

60. Fries, P. (2009). Neuronal gamma-band synchronization as a fundamental process in cortical computation. Annu. Rev. Neurosci. *32*, 209–224.

61. Muller, R.U., and Kubie, J.L. (1989). The firing of hippocampal place cells predicts the future position of freely moving rats. J. Neurosci. *9*, 4101–4110.

62. Battaglia, F.P., Sutherland, G.R., and McNaughton, B.L. (2004). Local sensory cues and place cell directionality: Additional evidence of prospective coding in the hippocampus. J. Neurosci. *24*, 4541–4550.

63. Bieri, K.W., Bobbitt, K.N., and Colgin, L.L. (2014). Slow and Fast Gamma Rhythms Coordinate Different Spatial Coding Modes in Hippocampal Place Cells. Neuron *82*, 670–681.

64. Yue, C., Remy, S., Su, H., Beck, H., and Yaari, Y. (2005). Journal of Neuroscience. J. Neurosci. *16*, 6676–6686.

65. Williams, S.R., and Stuart, G.J. (1999). Mechanisms and consequences of action potential burst firing in rat neocortical pyramidal neurons. J. Physiol. *521 Pt 2*, 467–482.

66. Yaari, Y., Yue, C., and Su, H. (2007). Recruitment of apical dendritic T-type Ca^{2+} channels by backpropagating spikes underlies *de novo* intrinsic bursting in hippocampal epileptogenesis. J. Physiol. *580*, 435–450.

67. Royer, S., Zemelman, B.V., Losonczy, A., Kim, J., Chance, F., Magee, J.C., and Buzsáki, G. (2012). Control of timing, rate and bursts of hippocampal place cells by dendritic and somatic inhibition. Nat. Neurosci. *15*, 769–775.

68. Chung, H., Park, K., Jang, H.J., Kohl, M.M., and Kwag, J. (2020). Dissociation of somatostatin and parvalbumin interneurons circuit dysfunctions underlying hippocampal theta and gamma oscillations impaired by amyloid β oligomers in vivo. Brain Struct. Funct. *225*, 935–954.

69. Cardin, J.A., Carlén, M., Meletis, K., Knoblich, U., Zhang, F., Deisseroth, K., Tsai, L.-H., and Moore, C.I. (2009). Driving fast-spiking cells induces gamma rhythm and controls sensory responses. Nature *459*, 663–667.

70. Larkum, M. (2013). A cellular mechanism for cortical associations: an organizing principle for the cerebral cortex. Trends Neurosci. *36*, 141–151.

71. Sheehan, D.J., Charczynski, S., Fordyce, B.A., Hasselmo, M.E., and Howard, M.W. (2021). A Compressed Representation of Spatial Distance in the Rodent hippocampus'. Preprint at bioRxiv. https://doi.org/10.1101/2021.02.15.431306.

72. Davoudi, H., and Foster, D.J. (2019). Acute silencing of hippocampal CA3 reveals a dominant role in place field responses. Nat. Neurosci. *22*, 337–342.

73. Berens, P. (2009). CircStat: A MATLAB toolbox for circular statistics. J. Stat. Softw. *31*, 1–21.

74. Brain-Observatory-Toolbox - File Exchange - MATLAB Central. https://de.mathworks.com/matlabcentral/fileexchange/90900-brain-observatory-toolbox.

75. Gritton, H.J., Howe, W.M., Romano, M.F., DiFeliceantonio, A.G., Kramer, M.A., Saligrama, V., Bucklin, M.E., Zemel, D., and Han, X. (2019). Unique contributions of parvalbumin and cholinergic interneurons in organizing striatal networks during movement. Nat. Neurosci. *22*, 586–597.

76. Hansen, K.R., Dewalt, G.J., Mohammed, A.I., Tseng, H., and Moona, E. (2017). Mild Blast Injury Produces Acute Changes in Basal Intracellular Calcium Levels and Activity Patterns in Mouse Hippocampal, *1–42*.

77. Pnevmatikakis, E.A., and Giovannucci, A. (2017). NoRMCorre: An online algorithm for piecewise rigid motion correction of calcium imaging data. J. Neurosci. Methods *291*, 83–94.

78. Oostenveld, R., Fries, P., Maris, E., and Schoffelen, J.-M. (2011). FieldTrip: Open source software for advanced analysis of MEG, EEG, and invasive electrophysiological data. Comput. Intell. Neurosci. *2011*, 156869.

79. Lachaux, J.-P., Lutz, A., Rudrauf, D., Cosmelli, D., Le Van Quyen, M., Martinerie, J., and Varela, F. (2002). Estimating the time-course of coherence between single-trial brain signals: an introduction to wavelet coherence. Neurophysiol. Clin. Neurophysiol. *32*, 157–174.

80. Aydore, S., Pantazis, D., and Leahy, R.M. (2013). A note on the phase locking value and its properties. Neuroimage *74*, 231–244.

81. Vinck, M., van Wingerden, M., Womelsdorf, T., Fries, P., and Pennartz, C.M.A. (2010). The pairwise phase consistency: A bias-free measure of rhythmic neuronal synchronization. Neuroimage *51*, 112–122.

82. Tejero-Cantero, A., Boelts, J., Deistler, M., Lueckmann, J.-M., Durkan, C., Gonçalves, P., Greenberg, D., and Macke, J. (2020). SBI – A toolkit for simulation-based inference. J. Open Source Softw. *5*, 2505.

STAR★METHODS

KEY RESOURCES TABLE

REAGENT or RESOURCE	SOURCE	IDENTIFIER
Bacterial and virus strains		
pAAV-Syn-SomArchon-GFP-P2A-CoChR-Kv2.1	UNC vector core	RRID: Addgene_126945
Deposited data		
pAAV-*syn*-SomArchon-BFP-P2A-CoChR-Kv2.1	Vigene Biosciences, Inc	RRID: Addgene_206006
Experimental models: Organisms/strains		
Mouse: C57BL6/J	Charles River Laboratories	RRID:MGI:5656552
Rat: Long-Evans	Charles River Laboratories	RRID:RGD_2308852
Software and algorithms		
Original code	This paper	https://github.com/HanLabBU/Lowet-Cell-Reports-2023
Adobe Illustrator	Adobe	RRID:SCR_10279
MATLAB	Mathworks	RRID:SCR_001622
HCImage	Hamamatsu Photonics	RRID:SCR_015041

RESOURCE AVAILABILITY

Lead contact
Further information and requests for code and data should be directed to the lead contact Xue Han (xuehan@bu.edu).

Materials availability
This study generated a new DNA plasmid, pAAV-Syn-SomArchon-mTagBFP2-p2A-CoChR-Kv2.1 (GenBank: OR336299).

Data and code availability
- Data are available from lead contact upon request.
- Codes used for data analysis is available on Github repository: https://github.com/HanLabBU/Lowet-Cell-Reports-2023. pAAV-Syn-SomArchon-mTagBFP2-p2A-CoChR-Kv2.1 DNA sequence is available at GenBank: OR336299.
- Any additional information required to reanalyze the data reported in this paper is available from the lead contact upon request.

EXPERIMENTAL MODEL AND SUBJECT DETAILS

All animal experiments were performed in accordance with the National Institute of Health Guide for Laboratory Animals and approved by the Boston University Institutional Animal Care and Use and Biosafety Committees. 4 male Long-Evans rats (Charles River Laboratories, Inc.), 350-500g, were used for all extracellular recording experiments.14 adult female C57BL/6 mice (Charles River Laboratories, Inc.), 8–12 weeks at the start of the study, were used for voltage imaging experiments. Since there were no comparisons between animal groups or behavioral tasks, no randomization of animals was implemented. Sample sizes for all experiments were determined based on previously published work, and statistical significance was determined post hoc.

METHOD DETAILS

Rat preparation for tetrode recordings. The surgical procedure was as described previously in detail.[71] Briefly, surgeries were performed under 1.5–3% isoflurane anesthesia (Webster Veterina Supply). Animals were injected with Buprenex (buprenorphine hydrochloride, 0.03 mg/kg, i.m.; Reckitt Benckiser Healthcare) and Cefazolin (330 mg/mL i.m.; West-Ward Pharmaceutical) preoperatively. Animals were implanted with custom unilateral microdrives containing 18–24 independently drivable tetrodes in the dorsal CA1 (AP: −3.6mm, ML: +2.6mm, from bregma). Animals received postoperative Buprenex and Cefazolin two times a day for 3 days.

    Extracellular tetrode recording. Extracellular recordings from custom tetrodes were recorded by a OmniPlex D Neural Acquisition System (Plexon). Each channel was amplified and bandpass filtered (154 Hz–8.8 kHz) to obtain both single-unit spike activity and LFPs (1.5 Hz–400 Hz). Spike channels were locally referenced to remove both movement-related noise and potential electrical noise.

Spikes were detected via threshold crossing and digitized at 40 kHz. To isolate single-units, waveform clusters from all four electrodes within a tetrode were manually identified using the Offline Sorter v3 (Plexon). Cineplex Studio (Plexon) was used for capturing animal location data via three infrared LEDs positioned atop the surgically implanted microdrive. Cineplex Editor (Plexon) was employed offline to enter event markers and to verify animal position data.

Extracellular spike burst (SB) detection. Given that we did not have access to membrane potentials for extracellular tetrode recordings, we identify SBs as periods of high frequency spiking with ISI less than 10ms. We chose a more conservative (smaller ISI) criterion for identifying SBs than for identifying SBs from voltage imaging recordings, because we did not have ADP-based criterion. Spikes not considered being part of any SB events were defined as single spikes. We only included neurons with mean firing rates below 20Hz estimated over the whole recording. There was a distinct subset of neurons, presumably fast-spiking interneurons, that exhibited very high tonic firing rates (small ISI), whose spikes were difficult to classify with an ISI-based criterion alone.

Spatial information and sparsity index

The amount of information a neuron has about the animal's position was defined as[24,72]:

$$\text{Spatial information} = \sum_{i=1}^{n} p_i \frac{f_i}{f} log_2 \frac{f_i}{f}$$

where p_i is the position bin probability defined as $p_i = t_i/\Sigma t_i$ (summed over i), t_i being the amount of time spent for a given spatial position bin. f is the mean firing rate defined as $f = \Sigma p_i f_i$.

$$\textit{Sparsity} = \frac{\left(\sum_{i=1}^{n} p_i f_i\right)^2}{\sum_{i=1}^{n} p_i f_i^2}$$

where f_i is firing rate of the neuron at the ith position bin.

Center of mass (COM) calculation

$$\text{COM} = \frac{\sum_{i=1}^{n} x_i f_i}{\sum_{i=1}^{n} f_i}$$

where x_i is the ith position bin on the linear track and f_i is firing rate of the neuron at the ith position bin.

Quantifying the relationship between Spike-LFP theta phase and position on linear track. For the place field theta spike phase analysis, we filtered the LFP signal in the theta (3-12Hz) frequency range using a butterworth filter kernel and zero-phase filter (built-in function butter and filtfilt, MATLAB). To obtain the instantaneous phase, we used the analytical signal of the Hilbert transform. To quantify the relationship between a neuron's preferred spike-LFP theta phase and animal's position, we applied circular-linear correlation[73] (CircStat toolbox, MATLAB) that estimates a coefficient of multiple correlation (analogues to the coefficient of determination, which is the square of the correlation value) ranging from 0 to 1 with 1 meaning all the variance is shared and 0 meaning no variation is shared.

Neuropixels mouse data. Freely accessible Neuropixels recording data from the Allen brain institute (Brain observatory 1.1) were used. Data were imported using the Brain observatory toolbox[74] and custom build MATLAB scripts. Only recording sessions with wild-type mice were included. Analysis was restricted to time periods when visual stimulus gratings of different orientations were shown to the animals (-1sec–3sec after stimulus onset). All neurons classified as CA1 neurons were included. For each recording session, a randomly chosen LFP contact from the Neuropixels probe was used for phase-locking analysis. SBs and SSs were classified in the same manner as for the rat tetrode recordings.

Mouse preparation for voltage imaging. Mouse preparation was as described previously.[31,75,76] Briefly, custom recording apparatus consists of an imaging window attached to an infusion cannula and an LFP electrode. The imaging window consists of a stainless-steel cannula (OD: 3.17mm, ID: 2.36mm, 1.75mm height, AmazonSupply, B004TUE45E) with a circular coverslip (#0, OD: 3mm, Deckgläser Cover Glasses, Warner Instruments Inc., 64–0726 (SB-3R-0)) adhered to the bottom using a UV curable adhesive (Norland Products Inc., Norland Optical Adhesive 60, P/N 6001). We attached an infusion cannula (26G, PlasticsOne Inc., C135GS-4/SPC), and a stainless-steel steel wire electrode for local field potential (LFP) recordings (Diameter: 130μm, PlasticsOne Inc., 005SW-30S, 7N003736501F) to the side of the imaging window using super glue (Henkel Corp., Loctite 414 and Loctite 713). The LFP electrode protruded from the bottom of the imaging window by ~200μm, whereas the drug infusion cannula was level with the base of the imaging window.

Recording apparatus was surgically implanted under 1–3% isoflurane anesthesia. Analgesia was provided with sustained release buprenorphine hydrochloride (0.03 mg/kg, i.m.; Reckitt Benckiser Healthcare) administered preoperatively that provided continued analgesia for 72 h. A craniotomy of ~3mm in diameter was made over the right dorsal CA1 (AP: -2mm, ML: +1.8mm). A small notch was made on the posterior edge of the craniotomy to accommodate the infusion cannula and the LFP recording electrode. The overlying cortex was gently aspirated using the corpus callosum as a landmark. The corpus callosum was then carefully thinned to expose the dorsal CA1. The imaging window was positioned in the craniotomy, and Kwik sil adhesive (World Precision Instruments LLC,

KWIK-SIL) was applied around the edges of the imaging window to hold it in place. A small ground pin was inserted into the posterior part of the brain near the lambda suture as a ground reference for LFP recordings. Three small screws (J.I. Morris Co., F000CE094) were anchored into the skull, and dental cement was then gently applied to affix the imaging window, the ground pin, and an aluminum headbar posterior to the imaging window. See Figure 3A for a diagram of recording apparatus placement.

AAV virus was infused via an infusion cannula (33G, PlasticsOne Inc., C315IS-4/SPC) connected to a microinfusion pump (World Precision Instruments LLC, UltraMicroPump3–4), through the implanted cannula. Infusion cannula terminated about 200μm below the imaging window. 500nL or 1000nL of AAVs were infused at a rate of 50-100 nL/min, and then the infusion cannula was left in place for another 10 min to facilitate AAV spread. AAVs used were AAV9-Syn-SomArchon-GFP (titer: 5.9e^{12} genome copies (GC)/mL, UNC vector core), AAV9-Syn-SomArchon-GFP-p2A-CoChR-Kv2.1 (titer: 5.9e^{12} GC/ml, UNC vector core) and AAV9-Syn-SomArchon-BFP-p2A-CoChR-Kv2.1 (titer: 1.53e^{13} GC/ml, Vigene Biosciences, Inc).

Single neuron SomArchon voltage imaging. Habituated mice were head-fixed on a custom air-pressured spherical Styrofoam ball and free to run. Animals were recorded 3–4 weeks after surgery. All single cell SomArchon imaging was acquired via a custom widefield fluorescence microscope equipped with either a Hamamatsu ORCA Fusion Digital sCMOS camera (Hamamatsu Photonics K.K., C14440-20UP) for 828Hz voltage imaging, or an ultra-high-speed sCMOS camera (Kinetix, Teledyne) operating at 8bit mode for 5kHz and 10kHz voltage imaging. A 40x NA 0.8 water immersion objective (Nikon, CFI APO NIR) was used. A 140mW fiber-coupled 637 nm laser (Coherent Obis 637-140X) was coupled to a reverse 2x beam expander (ThorLabs Inc., GBE02-E) to obtain a small illumination area of ∼30–40 μm in diameter to minimize background fluorescence. A mechanical shutter (Newport corp., model 76995) was positioned in the laser path to control the timing of illumination via an NI DAQ board (USB-6259, National instruments). The laser beam was coupled through a 620/60nm excitation filter (Chroma technology corp.) and a 650nm dichroic mirror (Chroma technology corp.), and SomArchon fluorescence emission was filtered with a 706/95nm filter (Chroma technology corp.).

GFP or BFP fused with SomArchon was used for localization of SomArchon expressing cells during each recording. GFP visualization was with a 470 nm LED (ThorLabs Inc., M470L3), an excitation 470/25nm filter, a 495nm dichroic mirror and a 525/50nm bandpass emission filter. BFP was visualized with a 395nm LED (ThorLabs Inc., M395L4), a 390/18nm excitation filter, a 416nm dichroic mirror and a 460/60nm emission filter. SomArchon fluorescence was either acquired at 828 Hz (16 bits, 2x2 binning), 5kHz or 10kHz, using HCImage Live (Hamamatsu Photonics). HC Image Live data were stored as DCAM image files (DCIMG) and analyzed offline with MATLAB (Mathworks Inc.). We did not detect notable differences for spike shape estimation for recordings performed at 5kHz versus 10kHz, and thus the imaging data were grouped together.

Multi-neuron SomArchon voltage imaging with patterned illumination. To record multiple CA1 neurons, a custom digital micromirror device based targeted illumination microscope was used as described previously.[34] In short, the custom-built widefield imaging scope includes a 6W 637 nm fiber-coupled multi-mode laser (Ushio America Inc., Necsel Red-HP-FC-63x), a digital micromirror device (DMD, Vialux, V-7000 VIS) and a high-speed and large sensor sCMOS (Hamamatsu, ORCA-Lightning C14120-20P). The laser output was collimated (Thorlabs, F950SMA-A), expanded (Thorlabs, BE02M-A), and directed onto the DMD. The DMD was controlled using a custom MATLAB script based on Vialux ALP-4.2 API. SomArchon fluorescence was acquired at 500 Hz (12bit) with 1152 × 576 pixels (2x2 binning), corresponding to a 360 × 180 μm^2 field of view. A subset of the CA1 multi-neuron imaging dataset was previously published[34] and was re-analyzed here.

Optogenetics. To excite CoChR, we used a blue 470 nm LED (ThorLabs Inc., M470L3) coupled to the laser path via a 416nm dichroic mirror, and controlled by T-Cube LED driver (ThorLabs Inc., LEDD18, lowest gain) controlled by MATLAB (Mathworks Inc.) via an NI DAQ board (USB-6259, National instruments). A neutral density filter (ThorLabs Inc., ND13A, optical density 1) was used to reduce LED illumination density. Further, we used a pinhole (Olympus BX3-URA8 fluorescence illuminator turret) to reduce the illumination to a circular area of 55μm radius under the 40x objective. For SomArchon-GFP-p2A-CoChR recordings, we used a LED intensity range of 0.22–1.3 mW/mm^2. For SomArchon-BFP-p2A-CoChR recordings, we used a higher LED intensity range of 2.6–8.4 mW/mm^2, because neural CoChR response was less sensitive to blue light stimulation likely due to lower CoChR expression. Simultaneous SomArchon and optogenetic recording trials consisted of 1 s period before blue light illumination, 1.5 s blue light illumination period, followed by 0.5 s period without blue light illumination. The 1.5-second-long blue light illumination was either continuous, or pulsed, at 40Hz (8.3ms per pulse) or 8Hz (8.3ms per pulse or 42ms per pulse). Inter-trial intervals were 5 s.

Local field potential (LFP) recording during voltage imaging. LFPs were recorded using the Open Ephys platform (http://open-ephys.org) at a 10 kHz sampling rate, filtered between 1Hz and 7.5kHz and then downsampled offline to 1kHz. To synchronize voltage imaging and LFP recordings during offline data analysis, the Open Ephys system also recorded the TTL pulses that were sent by the sCMOS camera at the onset of voltage imaging data acquisition as well as a TTL pulse at the onset of each image frame. Additionally, to align optogenetic stimulation timing with recordings, we also used the Open Ephys system to record the voltage that was used to control the blue LED driver during optogenetics.

Motion correction & neuron identification. SomArchon fluorescence images in DCMI format acquired by HCImage software were imported into MATLAB. SomArchon fluorescence images were first motion corrected using a pairwise rigid motion correction algorithm as described previously.[77] In short, the displacement of each image is computed by identifying the max cross-correlation coefficient between each image and the reference image. Our recordings consisted of multiple multi-second trials. For single-cell voltage imaging, each video file corresponding to one trial was first concatenated into a multi-trial image data matrix, and then we applied the motion correction algorithm. Since the illumination area is about 30-40μm in diameter, a rectangular window large enough to cover the entire neuron across all frames was selected manually for motion correction for single cell voltage imaging.

The window selection was chosen to avoid large regions of dark parts of image and to include regions that had distinguishable contrasts that facilitate comparison with reference image. For multi-cell voltage imaging, due to image file size, we did not concatenate the data across trials. Each trial was first motion corrected individually. We then corrected motion offsets across trials by referencing all trials to the first trial. The motion-corrected image sequences were then used for subsequent manual ROI neuron identification using the drawPolygon function in MATLAB. SomArchon fluorescence traces for each ROI were then extracted from the motion-corrected image sequences. Background fluorescence was estimated by averaging all pixels that are not part of the ROI. The traces were then detrended to correct for photobleaching by subtracting a low-pass filtered version of the trace (1.5sec rectangular smoothing kernel). The resulting fluorescence traces were then used for subsequent analysis.

Spike detection, subthreshold Vm trace extraction and spike signal-to-baseline ratio (SBR) calculation. Spike detection was performed similar to that described previously in Xiao et al.[34] To estimate the baseline, we first estimated baseline fluctuations by averaging the fluorescence trace using a moving window of ±100 frames to obtain the "Smoothed Trace" (ST). We then removed potential spike contributions to the baseline line by replacing fluorescence values above ST with the corresponding values of ST resulting in a spike-removed trace corresponding to the "subthreshold baseline fluctuations". To identify spikes, SomArchon fluorescence traces were high-pass filtered (>120Hz), and then spikes were detected as a fluorescence change greater than 4 standard deviations of the "subthreshold baseline fluctuations".

To extract subthreshold membrane voltage (Vm) fluctuations, we removed three data points centered at the peak of each detected spike from non-filtered SomArchon dF/F trace and interpolated the missing data points with the surrounding data points. To calculate spike signal-to-baseline ratio (SBR), we first obtained the spike amplitude by calculating the difference between the peak spike fluorescence and the lowest fluorescence value within three data points prior to the spike. We then divided the spike amplitude by the standard deviation of the Vm across the entire recording duration. To assure signal quality, only neurons with an averaged SBR of at least 4 were included for analysis.

Intracellular complex spike burst and single spike detection. A common way to identify bursting in extracellularly recorded single-unit data is to identify a cluster of spikes with short ISIs. However, ISI distributions for individual neurons are often continuous, and thus it is difficult to determine a definitive ISI threshold, leading to variation in ISI threshold of ~6-14ms across studies.[2,3,40] Recent intracellular studies demonstrated that individual spikes with SB can have ISIs of more than 10ms.[3] Thus, we used both ISI and Vm after-depolarization potential (ADP) to classify SB and SS. SB were detected as follows: First, putative spike bursts were detected based on ISI 14ms criterion and we classified each spike within a putative burst in terms of their order (1st spike, 2nd spike, etc.). ADP was calculated by the difference in the mean Vm during the 5-25ms period after the 1st burst spike and the mean Vm during the 5-25ms before the 1st burst spike, normalized by the averaged spike amplitude across the entire recording duration. If a putative burst had an ADP of more than 15%, it was considered as SB and all spikes of the burst was classified as SB spikes. Spikes that are not identified as SB were considered SS. SS could hence have ISI smaller than 14ms but are conceptualized here as high firing rate but regular spiking events.

Spike number matching for SB and SS in individual neurons. Phase-locking or coherence analysis can be biased by low spike number (<30) and lead to an inflation of values. As an additional control analysis, we matched the number of SBs and SSs for each neuron. For each neuron, a random set of spikes was eliminated from the spike type with the higher spike number (usually SSs, as there were typically more SSs than SBs), so that there are exactly the same number of SSs and SBs for further analysis.

Rank surprise-based SB detection algorithm. In addition to the ISI-based SB/SS classification approach, we also identified SB based on a 'surprise'-based algorithm[41] that detects SB as deviations from a Poisson distribution for a given neuron. Specifically, we chose a robust non-parametric rank-based approach (Gourévitch et al.,2007), in which the 'surprise' statistics is computed based on the ranks of ISIs.

Spectral decomposition. Spectral decomposition of SomArchon Vm or LFP was performed with FieldTrip MATLAB toolbox[78] (https://www.fieldtriptoolbox.org/), using wavelet morlets functions (5 cycles). The complex wavelets coefficients, from which we extracted the phase or power, were used to compute spike-LFP or spike-Vm phase locking values, and to estimate of the spectral power.

Spike phase-locking computation. To obtain a quantification of how consistent spikes occur relative to the phase of an oscillation we calculated the phase-locking value (PLV[79]) defined as:

$$PLV(f) \; = \; \left| \frac{1}{N} \sum_N e^{i\varphi(f,n)} \right|$$

where f is frequency and N is the total number of spikes. The phase φ was obtained from the complex wavelet spectrum.

Since PLV is not independent of the number of spikes considered and tends to inflate with low spike numbers. We only included neurons that had at least 10 spikes for spike-PLV analysis. Further, we adjusted the PLV value using the following equation[80,81] (mathematically equivalent to pairwise phase consistency) to account for any potential difference in the number of SB and SS detected in a neuron, which we term here as the unbiased squared phase locking value (PLVu^2):

$$PLVu^2(f) \; = \; \frac{1}{N-1} \left(PLV(f)^2 \; \times \; N - 1 \right)$$

where N is the number of spike occurrences and f is frequency. The unbiased PLVu^2 corresponds, at larger N, to the default PLV^2.

Finally, to further reduce any residual spike influence on PLV estimates from spike-removed SomArchon Vm traces, we shifted the spike train and the corresponding Vm trace by 8.2ms (7 frames at 828Hz sampling rate) to each other, which reduced the PLVu^2 inflation in the higher frequency range (>100Hz) due to spike number.

Simple biophysical bursting neuron model with four currents. The 2-compartment Hodgkin-Huxley model was constructed as that described previously.[9,12,13,42,43] In detail, the somatic membrane potential Vs. and dendritic membrane potential Vd are described by the two following equations:

$$C_m \frac{dVs}{dt} = -I_{leak} - I_{Na} - I_K - \frac{g_c(Vs - Vd)}{p} + I_{soma}$$

$$C_m \frac{dVd}{dt} = -I_{leak} - I_{NaP} - I_{KS} - \frac{g_c(Vd - Vs)}{1 - p} + I_{dend}$$

I$_{Na}$ and I$_K$ are the somatic/axon hillock spike generation sodium and potassium currents following standard Hodgkin-Huxley equations. I$_{Leak}$ is the leak current. The dendritic persistent sodium current I$_{NaP}$ and slowly activating potassium current I$_{KS}$ are responsible for the burst generation. The I$_{NaP}$ is described by following the equations:

$$I_{NaP} = g_{NaP} r_\infty^3 (V - E_{Na})$$

$$r_\infty(V) = 1 \left/ \left(1 + \left(-\frac{V+57.7}{7.7} \right) \right) \right.$$

The I$_{KS}$ is described by the following equations:

$$I_{KS} = g_{KS} q (V - E_K)$$

$$q_\infty(V) = 1 \left/ \left(1 + exp\left(-\frac{V+35}{6.5} \right) \right) \right.$$

$$\tau_q(V) = 200 \left/ \left(exp\left(-\frac{V+55}{30} \right) + exp\left(\frac{V+55}{30} \right) \right) \right.$$

Further: Cm = 1 μF/cm^2. The coupling between compartments had a g$_c$ = 1ms/cm^2. The relative area between somatic and dendritic compartment was p = 0.15 (soma area/full membrane area). Conductance values were: gKS = 0.8, gNaP = 0.08; gLeak = 0.18, gNA = 45 and gK = 20. The ionic reversal potentials were: E_Leak = −65mV, E_Na = +55mV, E_K = −90mV. Temperature scaling factor were Φ$_h$ = Φ$_n$ = 3.3; Φ$_m$ = 10. Numerical simulations were performed using Euler method with 0.01ms step size.

Non-bursting neuron model. The non-bursting neuron model was a classical 1-compartment Hodgkin-Huxley model with fast-acting potassium and sodium currents with kinetics as described above. For the simulations we used the 2-comparment model and set the compartment coupling to zero (g$_c$ = 0), which reduced the model a 1-compartment model (soma/axon) only.

Stimulus generation. The somatic compartment received a constant input. For Figure 7D, the dendritic input current consisted of theta and gamma signals as well as white noise. Theta was a sinusoidal with 7Hz frequency. Gamma was generated using filtered noise in the gamma range (70-80Hz). For Figure 7F, dendritic input consisted of white noise only.

To model place fields, the model neuron received an asymmetric dendritic input based on a previous theoretical study[55] and experimental evidences.[14] The input was increased linearly for 700ms and then decreased linearly 300ms to its baseline value. The input was further smoothed by averaging using a sliding window of 150ms. 40 trials were simulated with a theta rhythm of 8Hz with a variation of ±0.3Hz, and a gamma rhythmic input as described above.

Biophysical bursting model with a dendritic h-current. The two-compartment Hodgkin-Huxley[15] model included a somatic and a dendritic compartments. The first (somatic) compartment was taken from (Golomb et al., 2006[15]). The model included the currents that were known to exist in the soma and proximal dendrites of adult CA1 pyramidal cells: transient Na$^+$ (I$_{Na}$), delayed rectifier K$^+$ (I$_{Kdr}$), muscarinic-sensitive K$^+$ (I$_M$or I$_{Ks}$), persistent sodium (I$_{NaP}$), A-type K$^+$ (I$_A$), high-threshold Ca^{2+} (I$_{Ca}$), and two Ca^{2+}-activated K$^+$ currents, namely the fast Ca^{2+}-activated K$^+$ current (I$_C$) and the slow Ca^{2+}-activated K$^+$ current (I$_{sAHP}$). This model included, therefore, the most important currents known in somata and proximal axons of CA1 cells including INap and IM, which are responsible for somatic subthreshold theta resonance *in vitro*. The current balance equation for somatic compartment is

$$C \frac{dVs}{dt} = -gL(Vs - VL) - INa - INaP - IKdr - IA - IM$$

$$- ICa - IC - IsAHP + Iapp, s + ISD$$

where $Iapp, s$ is the applied current, ISD is the somato-dendritic coupling current.

The ionic voltage-dependent currents are described by: $INa(V, h) = gNam3\infty(V)h(V - VNa)$, $INaP(V) = gNaPp\infty(V)(V - VNa)$, $IKdr(V, n) = gKdrn4(V - VK)$, $IA(V, b) = gAa3\infty(V)b(V - VK)$, $IM(V, z) = gMz(V - VK)$.

The ionic calcium-dependent currents are described by: $ICa(V, r) = gCar2(V - VCa)$, $IC(V, c) = gCd\infty([Ca^{2+}]_i)c(V - VK)$, $IsAHP(V, q) = gsAHPq(V - VK)$.

We used sequential neural posterior estimation to adjust the model parameters with the experimental observations (Tejero-Cantero et al., 2020[82]). We have chosen 16 attributes from the observed signal to match with the model. This includes 4 moments from the membrane voltage, spike-train and interval statistics from both single and complex spikes, phase-locking values with respect to different frequency bands, and the resting potential mean and standard deviation which can be obtained outside of the stimulation window. As a result, we used the following estimated parameter values: $C = 1\mu F/cm2$ and $Iapp, s = 2.07 \mu A/Cm2$. The conductances and reversal potentials were: $g_L = 0.05$ mS/cm^2, $g_{Na} = 35$ mS/cm^2, $g_{NaP} = 0.92$ mS/cm^2, $g_{Kdr} = 6.13$ mS/cm^2, $g_A = 2.45$ mS/cm^2, $g_M = 2.49$ mS/cm^2, $V_L = -70$mV, $V_K = -90$mV and $V_{Na} = 55$mV.

For calcium currents: $g_{Ca} = 0.34$ mS/cm^2, $g_C = 14.47$ mS/cm^2, $g_{sAHP} = 11.52$ mS/cm^2, $V_{Ca} = 120$mV. The dynamic of the calcium concentration inside the cell, $[Ca^{2+}]_i$, was given by,

$$\frac{d[Ca^{2+}]_i}{dt} = -vICa - \frac{[Ca^{2+}]_i}{\tau Ca}$$

with $v = 0.13$cm^2/(ms $\times$ μA) and $\tau_{Ca} = 13$ms.

For the complete list of activation and inactivation curves we refer the reader to the table below:

Activation and inactivation curves $x_\infty(V)$ of somatic compartment, model from Golomb et al., 2006		
Current, variable	Kinetics/Time constant, ms	Parameters
INa, m	$m = m\infty(V)$	$\theta_m = -30$, $\sigma_m = 9.5$
INa, h	$dh/dt = (h\infty(V) - h)/\tau h(V)\tau h(V) = 0.1 + 0.75 \times \{1+exp[-(V - \theta ht)/\sigma ht]\}^{-1}$	$\theta_h = -45$, $\sigma_h = -7$ $\theta_{ht} = -40.5$, $\sigma_{ht} = -6.$
$INaP, p$	$p = p\infty(V)$	$\theta_p = -47$
$IKdr, n$	$dn/dt = (n\infty(V) - n)/\tau n(V)\tau n(V) = 0.1 + 0.5 \times \{1+exp[-(V - \theta nt)/\sigma nt]\}^{-1}$	$\theta_n = -35$, $\sigma_n = 10$, $\theta_{nt} = -27$, $\sigma_{nt} = -15$
$IKdr, a$	$a = a\infty(V)$	$\theta_a = -50$, $\sigma_a = 20$
$IKdr, b$	$db/dt = [b\infty(V) - b]/\tau b, \tau b = 15$	$\theta_b = -80$, $\sigma_b = -6$
IM, z	$dz/dt = [z\infty(V) - z]/\tau z, \tau z = 75$	$\theta_z = -39$, $\sigma_z = 5.$
Calcium currents		
ICa, r	$\frac{dr}{dt} = \frac{r\infty(V) - r}{\tau r}, \tau r = 1$ $r\infty(V) = \{1+exp[-(V - \theta r)/\sigma r]\}^{-1}$	$\theta_r = -20$, $\sigma_r = 10$
IC, c, d	$\frac{dc}{dt} = \frac{c\infty(V) - v}{\tau c}, \tau c = 2$ $d = d\infty([Ca^{2+}]_i)$ $c\infty(V) = \{1+exp[-(V - \theta c)/\sigma c]\}^{-1}$ $d\infty([Ca^{2+}]_i) = (1+ac/[Ca^{2+}]_i)^{-1}$	$\theta_c = -30$, $\sigma_c = 7$ $a_c = 6.$
$IsAHP, q$	$dq/dt = (q\infty([Ca^{2+}]_i) - q)/\tau q, \tau q = 450$ $q\infty([Ca^{2+}]_i) = (1+a4_q/[Ca^{2+}]_i^4)^{-1}$	$a_q = 2.$

The second (dendritic) compartment included an h-current. The current-balance equation was given by

$$C\frac{dV_d}{dt} = -gL(Vd - VL) - Ih + Iapp, d + IDS,$$

where the leak conductance is $g_L = 0.43$ mS/cm^2 and the current parameters are the same as in the first compartment, I_{DS} is the dendritic-somatic coupling current, $I_{app,d} = 0.3 \mu A/Cm2$ the applied current and I_h is an h-current given by $Ih = ghh(Vd - Vh)$. The dynamic of the h variable is given by

$$\frac{dh}{dt} = \frac{h_\infty(Vd) - h}{\tau h(Vd)} .$$

We used g_h = 4.4 mS/cm^2, V_h = 32.9mV. Also,

$$h\infty(V) = \left\{1+exp\left(\frac{V+84}{10.2}\right)\right\}^{-1}$$

and

$$\tau h(V) = \{exp(-17.9 - 0.116V)+exp(-1.84+0.09V)\}^{-1} + 0.1$$

these values were taken from (Gloveli et al., 2005).

The electrical coupling between the somatic and dendritic compartments were given by,

$$ISD = gsd(Vd - Vs) \text{ and } IDS = gds(Vs - Vd).$$

We used the same value for both conductances: g_{ds} = 0.2 and g_{sd} = 0.2.

The model is also driven by a white Gaussian noise current with zero mean and standard deviation 6.74. In addition, we include channel noise where the variable z also contains a white Gaussian noise in its formulation with zero mean and standard deviation 4.05×10^{-6}.

The code for this model is available at https://github.com/BioDatanamics-Lab/ca1_model.

NMDA current input incorporated into the h-current bursting model

According to a previous study by Grienberger et al. 2014,[53] it was found that intracellular complex spikes (CS) can also originate from the activation of NMDA receptors. For example, they showed that the 50ms current injection can induce CS (Fig S2. C1 of [53]), but CS disappeared after MK-801 addition (Fig S2. C2 of [53]). While NMDA mediated intracellular calcium rise is important for CS generation, the kinetics of NMDA is too slow to support theta and gamma frequencies. To test this hypothesis, we incorporated NMDA receptors into the dendritic compartment of the simple bursting h-current neuron model. NMDA current was modeled as described in Ermentrout&Terman[54] where the NMDA current was given by $I_{NMDA} = \overline{g}_{NMDA} \, s \, B(V) \, (V - V_{NMDA})$ with $B(V) = \left(1+\exp\left(-\frac{V - V_T}{16.13}\right)\right)^{-1}$ representing the magnesium block, and s the fraction of open channels given by,

$$\frac{ds}{dt} = a_r[T](1-s) - a_d s.$$

When a synaptic input is received, the value of $[T]$ jumps to T_{max} and then falls back to zero at the next time step. We used the parameters: a_r = 0.072 mM^{-1}ms^{-1}, a_d = 0.0066, V_{NMDA} = 0 mV, T_{max} = 1, and $\overline{g}_{NMDA}$ = 800. The I_{NMDA} input was only added in the dendritic compartment.

To provide non-rhythmic input, we used Poisson-distributed synaptic arrivals with homogeneous rates. For each rate, we conducted 20 trials of 1000ms each to compute the probability of observing an SB or an SS, using the same method described above. Additionally, we computed theta and gamma power by taking the mean value of the voltage power spectrum around 3-12Hz and 30-90Hz, respectively. The results in Figures S7d and S7e indicate that the number of SB indeed increases with NMDA activation, as suggested by Grienberger et al.[53]

QUANTIFICATION AND STATISTICAL ANALYSIS

All data analyses were performed using custom written MATLAB scripts (The Math Works). Paired and independent t-tests (all two-sided) were performed using standard built-in MATLAB functions. Linear regression was performed using built-in MATLAB function regress. For circular-linear correlation coefficient and significance, we used the algorithm from the MATLAB toolbox CircStat.[73]